Journal of Polymer Science

WILEY

JOURNAL OF POLYMER SCIENCE

RESEARCH ARTICLE OPEN ACCESS

The Role of Counterion Size in Defining Star-Shaped Polyelectrolytes Thermodynamics, Conformations, and Ion Dynamics

Andrea Tagliabue[1,2] | Massimo Mella[1]

[1]Dipartimento di Scienza ed Alta Tecnologia, Università degli Studi dell'Insubria, Como, Italy | [2]Dipartimento di Fisica, Università di Genova, Genoa, Italy

Correspondence: Andrea Tagliabue (andrea.tagliabue@edu.unige.it) | Massimo Mella (massimo.mella@uninsubria.it)

Received: 23 December 2024 | **Revised:** 10 March 2025 | **Accepted:** 14 March 2025

Keywords: counterions dynamics | ion exchange | Langevin simulation | polyelectrolyte | primitive coarse grain model

ABSTRACT

In this work, we systematically investigate the impact of counterion size on the behavior of star-shaped strong polyelectrolytes in dilute aqueous solutions using Langevin simulations and a primitive model of electrolytes. Varying both the counterion diameter and the number of arms of the polyelectrolyte, we demonstrate that both characteristics significantly impact polyelectrolyte conformations and counterion absorption. Counterion dynamics are also affected, the most interesting aspect being the presence of a fraction of mobile ions slowly diffusing, compared to the average behavior, which increases with polyelectrolyte branching and counterion size. Informed by the results on systems with single-size counterions, we also investigate possible changes in behavior of these polyelectrolytes when neutralized by a binary mixture of bulky and small counterions at different relative concentrations. Our results show that small counterions demonstrate a greater tendency for remaining located within the inner regions of the polyelectrolyte, particularly when their molar fraction is low and the polyelectrolyte is highly branched. This results in the spatial separation of the two species into core–shell-like structures, which dramatically decreases the diffusivity of the smaller counterions. By investigating the partitioning of counterions between the solution and the regions internal to the polyelectrolytes, it is shown that the selectivity toward the smaller species can be significantly enhanced by increasing the number of arms and operating under conditions of counterion scarcity.

1 | Introduction

Polyelectrolytes (PEs), i.e., polymers carrying either charged or ionizable monomeric units, exhibit highly responsive behavior that can be controlled by various solution properties, such as pH, temperature, solvent quality and screening power, as well as the concentration and nature of mobile ions present in solution. In particular, the latter can significantly influence the properties of PEs due to the stabilizing electrostatic interactions with the charged moieties on the chains, involving mechanisms governed by a balance between the energy gained from the condensation of counterions (CIs) and the associated change in entropy.

For instance, strong PEs are expected to decrease their extension upon the addition of salt ions to the solution, potentially undergoing collapse and eventually phase separation as attractive Coulomb interactions become stronger, particularly in the presence of multivalent CIs (see references [1, 2] for experimental results, and references [3–9] for theoretical findings) or oppositely charged species, leading to formation of gels [10, 11] or coacervates [12, 13].

In the case of weak PEs, their pK can be markedly decreased not only by increasing the screening power of the solution but also by adding ionic species capable of forming specific stabilizing interactions, coupled with electrostatic ones, such as hydrogen bonds [14] or hydrophobic interactions [15].

Although in many computational approaches the size of CIs is either completely neglected, as in mean-field approaches where mobile ions are represented as point-like charges, or assumed to be equal to that of monomers for convenience, it has been demonstrated both experimentally and through simulations that the radius of CIs often has a non-negligible impact on the behavior of PEs. In aqueous solutions, for instance, an increase in the excluded volume of CIs disfavors their accumulation along PE chains due to the diminished electrostatic interaction. Conversely, in low-polarity media, Coulomb attraction is strong enough to overcome the entropy-driven tendency of mobile ions to disperse in solution. In such cases, both theory and simulations suggest that condensation of bulky CIs can prevent the expected collapse of PEs [16–23].

These phenomena have significant implications for the behavior of various PE systems, as probed by focused experiments. For example, xanthan solutions above the critical concentration exhibit an increase in viscosity upon the addition of large cations, whether monovalent or divalent [24]. Furthermore, both strong and weak hydrogels may display different swelling behaviors upon ionization, depending on the CI size [25–28]. It has also been shown that the size of CIs influences the way in which PE-based systems self-assemble. For instance, neutral-β-charged diblock copolyelectrolytes exhibit various colloidal aggregate morphologies depending on the radius of their CIs [29, 30], with small ions promoting the formation of separated microphases, while bulky CIs increase the miscibility of the domains.

DNA also undergoes condensation phenomena depending on the hydration radius of divalent cations [31, 32], albeit the preferential interactions between DNA and small mobile cations remain debated [33–35]. Interestingly, Plesa et al. have shown that the pore translocation of knotted DNA is significantly affected when the monovalent cations in solution are changed from Li^+ to K^+ [36], an observation that can be attributed, at least in part, to the different sizes of the CIs and their solvation shells. This interpretation is further supported by a study on the impact of CI size on circular knotted PEs [37], which demonstrated that both small and bulky CIs favor knot localization, while medium-sized ones promote delocalized knots.

In conclusion, the size of CIs in PE systems has been shown to significantly impact outcomes in both theoretical/computational and experimental studies. However, most investigations have focused on linear PEs [16, 18, 20, 30, 38], and, to a minor extent, gels [25–28] and brushes [39–41], with relatively little attention given to branched chains, such as comb-like or star-shaped architectures. To the best of our knowledge, notable exceptions are the computational studies by Kłos and Paturej on charged dendrimers in the presence of CIs of different sizes [21, 22], which, however, primarily address the role of electrostatic interaction strength rather than the impact of the branching degree, and a very recent study by Aliakseyeu et al., which instead highlights how the star-like architecture slows down the dynamics of CIs of different types [42]. We thus hypothesize that chain architecture, particularly the degree of branching, may play a crucial role in how CIs of different sizes interact with the PE, influencing their condensation, absorption, and overall dynamical behavior within the system.

We base this idea also on previous experimental findings regarding the impact of changes in CI nature on the transport properties of hydrophilic PEs when the overall solution becomes crowded due to elevated macromolecular concentrations. In this context, substantially different viscosities have been measured following the substitution of Na^+ with tetra-alkyl ammonium ions in highly concentrated polystyrene sulfonate solutions [43], suggesting a substantially different degree of association between CIs and the PEs. Moreover, concentrated polylysine solutions exhibited significant variations in polymer diffusion constants upon changing the nature of anionic CIs [44], further indicating that differences in CI–chain interactions may impact transport properties due to both changes in solution viscosity and overall chain shape.

Thus, in this specific study, we conduct a systematic investigation of the impact of CI size on star shaped strong PEs with varying numbers of arms, f. Specifically, we first examine how CI diameter, σ_{CI}, influences the conformational properties of the PE as a function of f, as well as the CI dynamics and thermodynamics of condensation and absorption. We anticipate that CI size significantly affects all the properties investigated, among which the effective (i.e., partially compensated by CI absorption) charge of the PE. Hinging on the information obtained for systems with CIs of homogeneous size, we also explore how the behavior of the PE is further modified in the presence of a binary mixture of small and bulky CIs, varying the ratio between the two species to examine possible changes in absorption selectivity. Notably, unlike previous studies [16, 18], which assumed the same friction acting on all species regardless of their size, we implement a size-dependent friction model that more accurately simulates the dynamics in a viscous medium. This approach allows us to demonstrate that the CI dynamics is affected in a nontrivial way, particularly in the presence of mixtures of small and bulky CIs, and that accounting for or neglecting the different drag experienced by the species leads to dramatically different results.

2 | Model and Methods

In this section, we describe the polyelectrolyte model implemented and the methods employed to investigate the behavior of the simulated systems. Given the large number of symbols and variables involved in the discussion, we provide a list of the most frequently used ones in the Supporting Information (SI); see Tables S1 and S2.

2.1 | Model

The simulated system consists of a single star-shaped polyelectrolyte (PE, or "star") in a periodically repeated cubic cell, with a side length set to yield a molar concentration of charged monomers equal to 10^{-2} mol/L. Each arm is represented via a coarse-grained "beads–springs" primitive model and consists of f linear

chains ("arms") composed of L negatively charged monomers. Bonds between consecutive beads in each arm are modeled via a finitely extensible nonlinear elastic (FENE) potential,

$$U_{\mathrm{FENE}}(r_{ij}) = -\frac{1}{2}k_{\mathrm{bond}}r_{\mathrm{max}}^2 \ln\left(1-\left(\frac{r_{ij}}{r_{\mathrm{max}}}\right)^2\right), \quad (1)$$

where r_{ij} is the distance between bonded monomers i and j, $r_{\mathrm{max}} = 3\sigma$ is the maximum allowed bond elongation, and $k_{\mathrm{bond}} = 60\epsilon/\sigma^2$ is the force constant. In this expression, the potential depth ε is set equal to the the characteristic thermal energy of the system, $k_{\mathrm{B}}T$, which is in canonical equilibrium at temperature T. The r_{max} and k_{bond} values correspond to an alternative parametrization of the standard Kremer–Grest model [45] yielding a practically indistinguishable effective bonding potential up to several $k_{\mathrm{B}}T$ units from the minimum [37]. The first monomer of each arm is connected to a central neutral monomer ("star center") using the same bonding potential.

The charge of the PE is neutralized by the presence of $N_{\mathrm{CI}} = fL$ monovalent-positive CIs. Electrostatic interactions are represented using the Coulomb potential,

$$U_{\mathrm{Coul}}(r_{ij}) = \frac{1}{4\pi\varepsilon_0\varepsilon_r}\frac{e^2 z_i z_j}{r_{ij}} = z_i z_j k_{\mathrm{B}}T\frac{l_{\mathrm{B}}}{r}, \quad (2)$$

and are handled using the P^{3}M method, with an accuracy set to 10^{-3}. In Equation (2), r_{ij} is the distance between two interacting particles i and j, e is the elementary charge, z_i and z_j are the signed charge valencies of the two particles, ε_0 is the vacuum dielectric constant, and ε_r is the relative permittivity of the medium. The solvent is represented by a uniform dielectric continuum, so its molecular structure is neglected. Setting $\sigma = 3.55$ Å results in a Bjerrum length approximately equal to that of pure water at room temperature, i.e., $\varepsilon_r \approx 78$ and $l_{\mathrm{B}} = e^2/(4\pi\varepsilon_0\varepsilon_r k_{\mathrm{B}}T) = 2\sigma = 7.10$ Å.

Excluded volume interactions between all pairs of particles are represented as soft spheres via a Weeks–Chandler–Anderson (WCA) potential [46], given by

$$U_{\mathrm{WCA}}(r_{\mathrm{ij}},\sigma_{\mathrm{ij}}) = \begin{cases} 4\epsilon\left[\left(\frac{\sigma_{\mathrm{ij}}}{r_{\mathrm{ij}}}\right)^{12} - \left(\frac{\sigma_{\mathrm{ij}}}{r_{\mathrm{ij}}}\right)^{6} + \frac{1}{4}\right] & \text{if } r_{\mathrm{ij}} < r_{\mathrm{cut}} \\ 0 & \text{otherwise} \end{cases} \quad (3)$$

where $r_{\mathrm{cut}} = 2^{\frac{1}{6}}\sigma_{ij}$ is the cutoff radius, and $\sigma_{ij} = \frac{1}{2}(\sigma_i + \sigma_j)$ is a parameter defining the WCA interaction between two particles i and j with diameters σ_i and σ_j, respectively. The diameter of the charged monomers, σ_{mono}, and the star center, σ_{N}, are set equal to σ, wheres the diameter of the CIs, σ_{CI}, is varied in the range $[0.5\sigma, 2.5\sigma]$. For simplicity, we introduce dimensionless parameters by adding the superscript "$*$", e.g., $\sigma_{\mathrm{CI}}^* = \sigma_{\mathrm{CI}}/\sigma$.

2.2 | Simulation Protocol

In this study, we explore star PEs with $f = 2$, 4, 8, and 15 arms. The length of each arm is fixed at $L = 20$, while the total number of monomers, $N_{\mathrm{mono}} = fL + 1$, varies accordingly. The number of counterions, $N_{\mathrm{CI}} = fL$, also varies, and the box volume is adjusted to maintain a monomer concentration of $C_{\mathrm{mono}} = 10^{-2}$ mol/L. A few simulations with a fixed total number of monomers and CIs, thus varying the arm length, showed no qualitative differences in trends with respect to f and σ_{CI}.

The systems are evolved via Langevin dynamics simulations, described by the equation,

$$m_i\ddot{\mathbf{x}}_i = -\gamma_i\dot{\mathbf{x}}_i + \mathbf{F}_i + \mathbf{R}_i, \quad (4)$$

where m_i, $\dot{\mathbf{x}}_i$, and $\ddot{\mathbf{x}}_i$ represent, respectively, the mass, velocity, and acceleration of the i-th particle, while γ_i, $\mathbf{F}_i$, and $\mathbf{R}_i$ are, respectively, the friction coefficient, the conservative forces, and the random forces acting on it. The latter act on each particle independently and obey the fluctuation-dissipation theorem. Differently from previous studies, which analyze CI dynamics as a function of their size [16, 18] but do not account for different friction forces on differently sized beads, we implement a size-dependent friction, $\gamma_y = \frac{\sigma_y}{\sigma}\frac{1}{(m\epsilon)^{1/2}}$ (hence, $\gamma_y^* \equiv \sigma_y^*$), where y represents the species considered. This allows us to more accurately capture the impact of bead diameter on the frictional dissipation and the associated thermal fluctuations, ensuring that larger particles experience greater friction, in line with their increased drag. Thus, our simulations offer a more realistic representation of the differently sized CIs in motion. However, we point out that the use of the Langevin thermostat corresponds to the Rouse (i.e., fully draining) chain dynamics [47], which does not explicitly account for hydrodynamic interactions. Nevertheless, the relative dynamics of the CIs with respect to the star PE is expected to be, at least qualitatively, well described under the assumption that electrostatic interactions dominate and hydrodynamic effects play a less significant role. In order to evaluate the impact of accounting a size-dependent friction, simulations with a uniform friction value (i.e., $\gamma_y^* \equiv \gamma^* = 1\,\forall y$), have also been run.

Two sets of simulations were performed:

i. In the first set, the diameter of CIs was varied in the range $\sigma_{\mathrm{CI}}^* \in [0.5, 2.5]$.
ii. In the second set, two species of CIs with different diameter values, $\sigma_{\mathrm{s}}^* = 0.5$ and $\sigma_{\mathrm{B}}^* = 2.0$ ("s" denotes "small" and "B" denotes "bulky"), were present with tunable molar fractions χ_{s} and $\chi_{\mathrm{B}} = 1 - \chi_{\mathrm{s}}$.

Importantly, the chosen relative diameter values are consistent with experimentally accessible species, as the size of monovalent cations may be easily varied, for instance, by using ammonium ions bearing different alkyl groups [48].

All simulations were performed with the software package ESPResSo 4.1 [49], using default values for the mass of the particles, m. The dynamics were integrated with a velocity Verlet algorithm using a time step $\delta t = 0.01\tau_{\mathrm{LJ}}$, where $\tau_{\mathrm{LJ}} = \sigma\sqrt{(m/\varepsilon)}$ is the Lennard–Jones time.

For each set of system parameters, we collected at least five independent trajectories, each with a duration of $t_{\mathrm{sim}} = 10^5\tau_{\mathrm{LJ}}$, following an

initial relaxation stage of duration $t_{\text{therm}} = 2 \times 10^3 \tau_{\text{LJ}}$. Canonical expectation values of the system properties were computed over configurations sampled at intervals of $t_{\text{sample}} = 20\tau_{\text{LJ}}$, and are denoted by angular brackets, $\langle \cdot \rangle$. Mean values are presented with their standard errors, averaged over the independent trajectories, and are smaller than the plot symbols when not visible.

2.3 | Conformational and Thermodynamical Analysis

2.3.1 | Radius of Gyration and Arm Extension

The size of a polymeric chain can be described by its squared gyration radius,

$$R_{\text{g}}^2 = \sum_{i=1}^{N_{\text{mono}}} \frac{\left(\mathbf{x}_{\text{CoM}} - \mathbf{x}_i\right)^2}{N_{\text{mono}}}, \tag{5}$$

where $\mathbf{x}_i$ and $\mathbf{x}_{\text{CoM}}$ are the coordinate vectors of, respectively, the i-th monomer and the center of mass of the chain.

Another commonly used property for characterizing the size of a linear polymer is the "end-to-end" distance, i.e., the distance between the first and the last monomer of a chain. This quantity can be easily extended to star-shaped PEs. Thus, we define the squared "arm extension" of a given arm j as,

$$\ell_{\text{a},j}^2 = \left(\mathbf{x}_{\text{N}} - \mathbf{x}_{\text{last}}\right)^2, \tag{6}$$

where $\mathbf{x}_{\text{N}}$ and $\mathbf{x}_{\text{last}}$ are the coordinate vectors of, respectively, the star center and the last monomer of the j-th arm. We denote the instantaneous (i.e., at a time $t = t_0$) root mean square value of the arm extension averaged across all the f chains as,

$$\overline{\ell}_{\text{a}} = \sqrt{\sum_{j=1}^{f} \frac{\ell_{\text{a},j}^2}{f}}, \tag{7}$$

to distinguish it from the root mean square value obtained by averaging over the simulation time, $\sqrt{\langle \ell_{\text{a}}^2 \rangle}$.

2.3.2 | Counterion Condensation and Absorption

We say that a CI c is *condensed* (or *ad*sorbed) on the PE if there is at least one monomer m such that the distance between c and m is less than or equal to an arbitrary cutoff r_{cond}. Unlike similar studies in the literature, we set $r_{\text{cond}} = l_{\text{B}} = 2\sigma$ regardless the size of the CIs considered. This choice allows us to establish a criterion based solely on energetic arguments: the distance at which the attraction between two oppositely charged species equals the thermal energy. We denote the number of condensed CIs as υ, and the fraction of condensed CIs as $\varphi = \upsilon / N_{\text{CI}}$. This fraction also represents the number of condensed CIs per charged monomer.

Similarly, we say that a CI c is *ab*sorbed into the star if it is located at a distance from the star center, r, less than the average arm extension, i.e., $r < \overline{\ell}_{\text{a}}$. The number and the fraction of absorbed CIs are denoted by, respectively, Υ and Φ. It is worth noting that the latter provide meaningful metrics for quantifying the amount of adsorbed CIs only if the shape of the PE can be reasonably approximated as a sphere. Consequently, these quantities were not calculated for the case $f = 2$. Furthermore, we define $\mathcal{Z}_{\text{eff}} \approx N_{\text{mono}} + \Upsilon = N_{\text{mono}}(1 + \Phi)$ as the effective charge exhibited by the PE upon CI absorption.

When dealing with a binary mixture of CIs of different sizes (with diameters σ_{s} and σ_{B}, respectively), we will use subscripts to uniquely identify each species. Thus, φ_{s} and Φ_{s} denote the fraction of *small* CIs that are condensed on and absorbed by the PE, respectively. It is important to note that, when calculating these fractions, the denominator can be either the total number of CIs, N_{CI}, or the number of small CIs, $N_{\text{s}} = \chi_{\text{s}} N_{\text{CI}}$. For convenience, we denote as φ_{y} and Φ_{y} (y = "s" or "B") the fractions computed using the total number of CIs as the denominator, and as $\varphi_y^{(\chi)}$ and $\Phi_y^{(\chi)}$ the fractions computed using the number of, respectively, small and bulky CIs.

Finally, to investigate how CIs are distributed inside and around the star, we compute the radial distribution function of monomer and CIs, $g(r)$, with respect to the star center. To facilitate comparison across systems with different numbers of particles, we define the quantity $g'(r) = \rho_{\text{CI}} g(r)$, where ρ_{CI} is the absolute density of CIs. Additionally, by "inverting" $g(r)$, we derive the Helmholtz energy profile of the CIs as a function of their distance from the star center. This profile represents the reversible work, $w_{\text{rev}}(r)$, required to move a particle from the bulk (i.e., from $r \to \infty$, approximated as half the side of the simulation cell for convenience) to a distance r from the star center.

2.3.3 | Polyelectrolyte Selectivity Toward Counterions of Different Sizes

In the presence of a binary mixture of small and bulky CIs, preferential condensation of one species over the other may occur. To quantify this phenomenon, one can compute the *selectivity* of the PE toward small CIs condensation as follows:

$$S_{\text{s}}^{(\varphi)} = \frac{\varphi_{\text{s}}^{(\chi)}}{1 - \varphi_{\text{s}}^{(\chi)}} \frac{1 - \varphi_{\text{B}}^{(\chi)}}{\varphi_{\text{B}}^{(\chi)}} \tag{8}$$

This formulation is analogous to the selectivity measure commonly used in the study of gas mixture adsorption on solid substrates [50].

However, accurate computation of $S_{\text{s}}^{(\varphi)}$ is hindered by the finite size of the system. Specifically, we anticipate that when $\chi_{\text{s}} \ll \chi_{\text{B}}$, small CIs might be fully condensed within the PE (thus $\varphi_{\text{s}}^{(\chi)} \to 0$) potentially leading to their absence in the bulk. To address this issue without resorting to larger simulations, we approximate the average selectivity toward small CIs as,

$$\left\langle S_{\text{s}}^{(\varphi)} \right\rangle \approx \left\langle \frac{\left\langle \varphi_{\text{s}}^{(\chi)} \right\rangle_j}{1 - \left\langle \varphi_{\text{s}}^{(\chi)} \right\rangle_j} \frac{1 - \left\langle \varphi_{\text{B}}^{(\chi)} \right\rangle_j}{\left\langle \varphi_{\text{B}}^{(\chi)} \right\rangle_j} \right\rangle \tag{9}$$

where $\langle \cdot \rangle_j$ are the mean values obtained averaging over the j-th trajectory. Although this approximation may not correctly

reflect the actual average value, it remains valuable for assessing semiquantitative differences in selectivity between species as a function of mixture composition and PE architecture, thus allowing for effective comparison and interpretation of the relative affinities of different CI species within the systems.

It is important to note that the expression provided in Equation (9) represents the selectivity toward small CI upon condensation. Obviously, an analogous expression can be used to define the selectivity upon small CI absorption:

$$\left\langle S_{\mathrm{s}}^{(\Phi)} \right\rangle \approx \left\langle \frac{\left\langle \Phi_{\mathrm{s}}^{(\chi)} \right\rangle_j}{1-\left\langle \Phi_{\mathrm{s}}^{(\chi)} \right\rangle_j} \frac{1-\left\langle \Phi_{\mathrm{B}}^{(\chi)} \right\rangle_j}{\left\langle \Phi_{\mathrm{B}}^{(\chi)} \right\rangle_j} \right\rangle. \tag{10}$$

2.4 | Counterion Dynamics

With the aim of shedding light on the impact of σ_{CI} on CI dynamics, we computed their mean squared displacement (MSD). The MSD of a given CI is calculated using a "sliding window" approach, i.e., it is averaged over all possible lag times $t_{\mathrm{sample}} \leq \Delta t \leq t_{\mathrm{sim}}/4$:

$$\mathrm{MSD}(c,\ \Delta t) = \left\langle \frac{1}{N_{\Delta t}} \sum_{i=1}^{N_{\Delta t}} \left[\mathbf{r}_c(i\Delta t) - \mathbf{r}_c(i\Delta t - \Delta t) \right]^2 \right\rangle \tag{11}$$

Here, $N_{\Delta t}$ is the number of non-overlapping time intervals of length Δt, whereas $\mathbf{r}_c$ is the position of the counterion c with respect to the star center. Thus, we avoid the overlapping windows of the same size but rather considers different nonoverlapping time intervals, thereby maximizing the number of samples while minimizing correlations between them. It is also worth noting that, since the central monomer is fixed at the center of the simulation box, the MSD curves are calculated relative to the star center. Besides the MSD of individual CIs, we also provide the average MSD computed across all CIs and all independent trajectories. From the latter, we determine the diffusion coefficient D by linearly fitting the terminal portion of the average MSD curve.

Eventually, we compute the CI absorption lifetime, τ_{abs}, i.e., the amount of time that is elapsed from the absorption of a CI until its release back into the solution, and its distribution to quantify the rate of CI exchange between the bulk solution and the space occupied by the PE.

3 | Results

3.1 | Impact of Counterions Size

3.1.1 | Conformational and Thermodynamical Analysis

We start our discussion by analyzing the selected trajectory snapshots of systems with different numbers of arms and CI diameters reported in Figure 1. From visual inspection, we observe that:

i. As the diameter of CIs, σ_{CI}, increases, the linear charged arms progressively straighten, reflecting an increase in their persistence length and, consequently, enhanced effective bending rigidity. Overall, the size of the PE grows with both the number of arms, f, and σ_{CI}.

ii. The number of CIs condensed on the chain increases with the number of arms, f, and decreases with σ_{CI}.

The observation made in item (i) are supported by the data reported in Figure 2a, which illustrates the dependence of the root

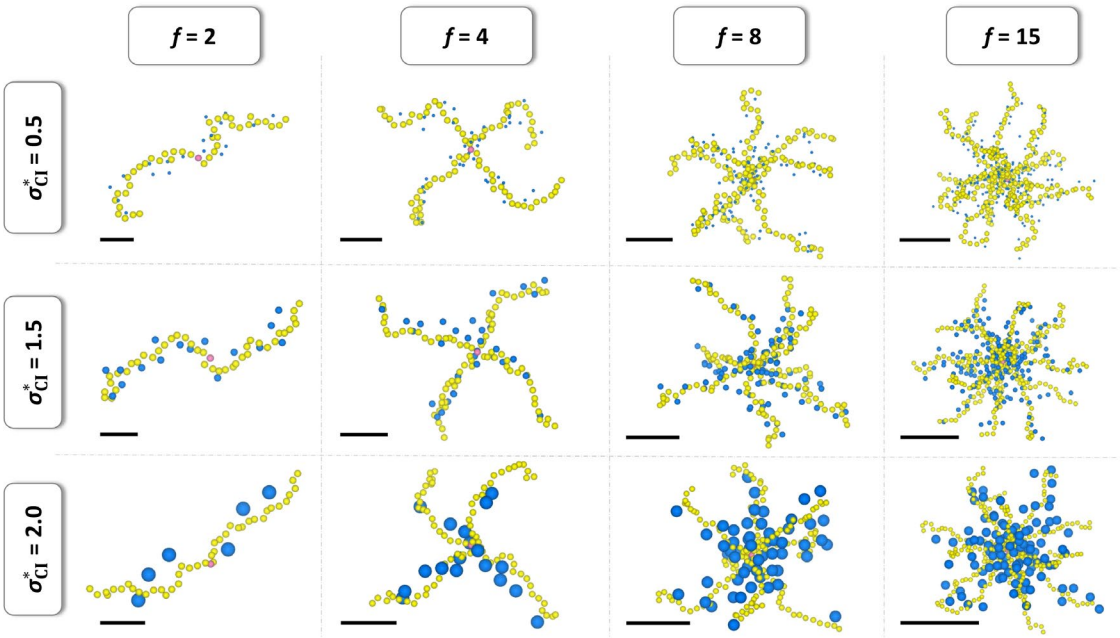

FIGURE 1 | Trajectory snapshots of star PEs with various numbers of arms and CI sizes. Color scheme: Central monomer in pink, charged monomers in yellow, CIs in blue. For clarity, only *condensed* CIs are shown, and bonds between monomers are omitted to reduce visual clutter. As the conformations are not to scale, each snapshot includes a black bar proportional to the $\left\langle R_{\mathrm{g}}^2 \right\rangle$ value to provide a sense of scale.

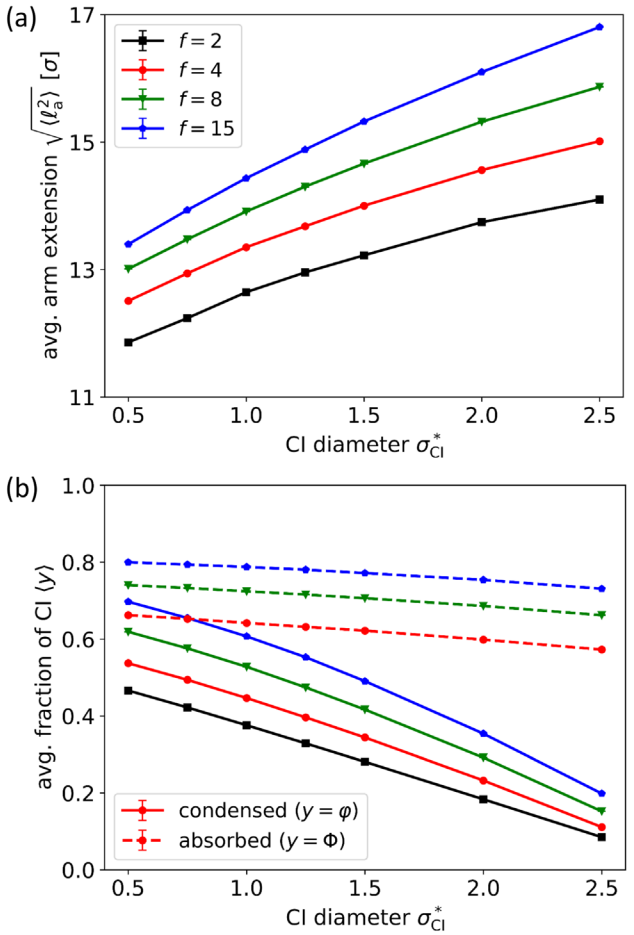

FIGURE 2 | (a) Root mean square arm extension and (b) fraction of condensed (solid lines) and absorbed (dashed) CIs plotted against the CI diameter.

mean square arm extension, $\sqrt{\langle \ell_a^2 \rangle}$, on the diameter of CIs. Qualitatively similar trends are observed in the $\sqrt{\langle R_g^2 \rangle}$ versus σ_{CI} curves reported in Figure S2. At fixed σ_{CI}, $\sqrt{\langle \ell_a^2 \rangle}$ increases with the number of arms due to the enhanced rigidity induced by electrostatic intra-arm repulsion—a phenomenon extensively discussed in literature (see, e.g., reference [37]). The extent of this effect depends on σ_{CI} because small CIs tend to "wrinkle" the chain to maximize contact with neighboring monomers, a capability that diminishes as σ_{CI} increases. Indeed, wrapping around a bulky CI not only requires the charged segment to adopt conformations with a higher persistence length to adhere to the CI's surface (compared to a small one) but also involves a greater number of monomers (i.e., a longer charged segment). Importantly, due to the star-shaped architecture of our PEs, the presence of condensed CIs along the chains not only diminishes their persistence length but also reduces the effective interaction between arms (which, in turn, grows with f).

The insights from item (ii) are instead supported by Figure 2b, which shows the average fraction of CIs condensed and absorbed, $\langle \varphi \rangle$ and $\langle \Phi \rangle$ respectively, plotted against σ_{CI}. First, focusing on the fraction of condensed CIs, the increase in $\langle \varphi \rangle$ with the number of arms, f, can be attributed to the higher charge density resulting from the increased branching of the PE. On the other hand, the decrease in $\langle \varphi \rangle$ with increasing σ_{CI} is due to larger CIs losing their ability to condense close to the charged chains. This reduction is not only attributed to a weakening of the attractive electrostatic interactions but also to the reduced ability of larger CIs to penetrate and accumulate within the inner regions of the star-shaped structure (*vide infra* the radial distribution function shown in Figure 3a–d). This explanation clarifies why the slope of the $\langle \varphi \rangle$ versus σ_{CI} curves increases with the number of arms (see also Figure S3), indicating that higher σ_{CI} more effectively hinders CI condensation in highly branched stars, especially within their innermost regions.

While the amount of condensed CIs decreases significantly with increasing σ_{CI}, the fraction of absorbed CIs, $\langle \Phi \rangle$, decreases only slightly. This suggests that as CIs grow larger, they detach from the charged chains but remain within the volume swept by the star PE, $\langle V^{(abs)} \rangle$. Exploiting the result on the root mean squared arm extension to approximate the accessible star volume, we get $\langle V^{(abs)} \rangle \approx \frac{4}{3}\pi\left(\langle \ell_a^2 \rangle^{3/2} - N_{mono}\sigma_m^3\right)$, which increases with both σ_{CI} and f, see Figure S4. This increase is due to the linearization of arms caused by both the excluded volume of bulky CIs and inter-arm repulsion. As an example, for a star with 15 arms, $\langle V^{(abs)} \rangle$ increases by about 111 % when moving from very small ($\sigma_{CI}^* = 0.5$) to bulky ($\sigma_{CI}^* = 2.5$) CIs. Additionally, by including the absorbed CIs in the total charge count of the PE/CIs complex, we observe that the net charge, $\mathcal{Z}_{eff}$, decreases by about 60%–80% compared to the bare star, depending on f and σ_{CI} values (Figure S5).

Importantly, the differences in the condensation and absorption of differently sized CIs are expected to reflect in variations in the system's osmotic pressure [51, 52]. This is illustrated by the results in Figure S6, which shows how the system's average virial pressure [53, 54], $\langle p \rangle$, varies with σ_{CI} for differently branched PEs. Specifically, $\langle p \rangle$ increases with σ_{CI} and decreases with the number of arms f, reflecting the trends observed in the condensation and absorption profiles discussed earlier.

To gain insights into how the CIs distributes inside and around the star, the top panels of Figure 3 show the radial distribution functions of CIs, $g'(r)$, calculated relative to the position of the star center for systems with different numbers of arms and CI diameters. We observe that the $g'(r)$ profiles exhibit a pronounced peak near the center of the star, its exact location depending on σ_{CI}. As expected, these peaks consistently occur at distances $r_1 > \left(\sigma_{CI}^* + \sigma_N^*\right)/2$, with the deviation from this value increasing with both f and σ_{CI}.

As f increases, the height of the main peak in $g'(r)$ also grows, reflecting the greater number of condensed and absorbed CIs. Conversely, increasing σ_{CI} while keeping f constant leads to a gradual exclusion of CIs from the star center due to excluded volume effects. Additionally, secondary features such as local maxima or shoulders appear in the $g'(r)$ profiles. For instance, at $f = 15$ and $\sigma_{CI}^* = 0.5$, a secondary peak emerges very close to the star center, i.e., at $r \approx \left(\sigma_{CI} + \sigma_N\right)/2 < r_1$, suggesting that small CIs can be absorbed between the central bead and the charged monomers directly bonded to it. Conversely, for $\sigma_{CI}^* = 2.5$ and $f \geq 8$, we observe a secondary peak (a marked shoulder at $f = 4$)

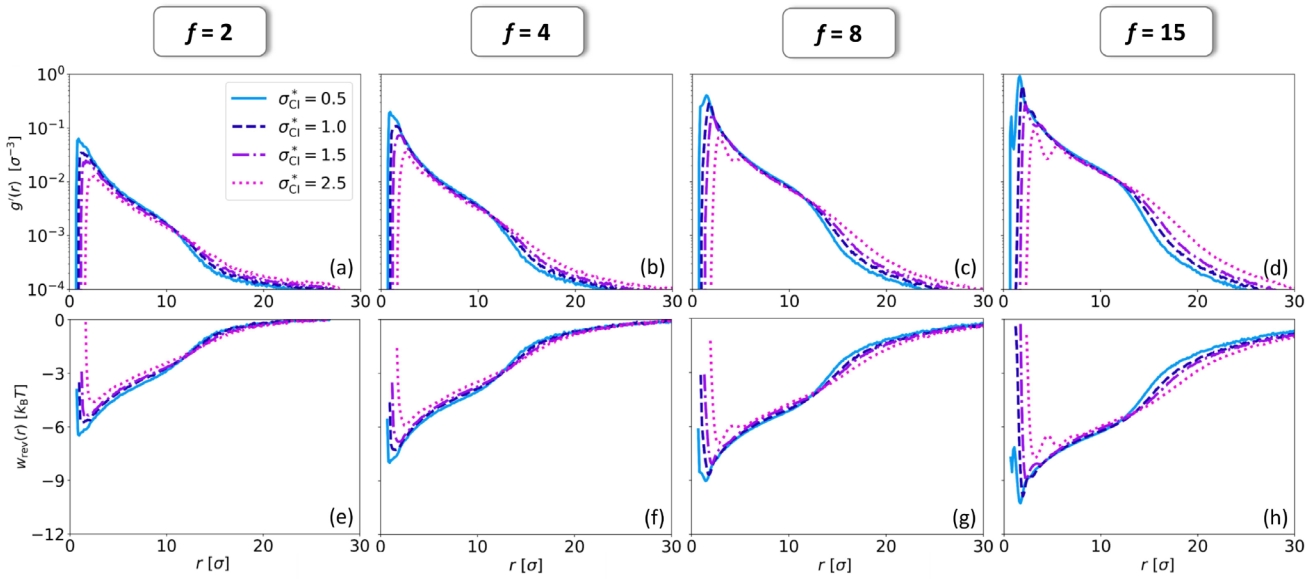

FIGURE 3 | (a–d) Radial distribution functions of CIs relative to the star center. (e–h) Amount of reversible work required to move a CI from the bulk to a distance r from the star center.

at distances $r > r_1$, indicating a secondary shell of accumulation roughly corresponding to the position of the sixth monomer from the star center; see also the $g'(r)$ of charged monomers, Figure S7. Importantly, the angular averaging inherent in these profiles may underestimate the CI density along the arm directions and overestimate it in the perpendicular directions.

By using the radial distribution functions of the CIs and invoking the potential of mean force theorem [55], we can compute the (angularly averaged) reversible work, $w_{rev}(r)$, required to bring a CI from the bulk to a distance r from the star center. For convenience, the curves are shifted so that $w_{rev}(r) = 0$ at a distance equal to half the length of the box side. The results are displayed in the lower panels of Figure 3. For the case $f = 2$, $w_{rev}(r = r_1)$ is approximately in the range $(-6.5, -4.5)\ k_BT$ depending on the size of the CIs, with an energetic advantage of about $-2k_BT = -1.2$ kcal/mol when adsorbing small CIs ($\sigma^*_{CI} = 0.5$) in comparison to bulky ones ($\sigma^*_{CI} = 2.5$). As f increases, the magnitude of $w_{rev}(r = r_1)$ also grows. For instance, when $f = 15$, $w_{rev}(r = r_1) \simeq -10.5k_BT$ for $\sigma^*_{CI} = 0.5$, while it is about $-7.5k_BT$ for $\sigma^*_{CI} = 2.5$. This results in an energetic gain of approximately $-3k_BT = -1.8$ kcal/mol when small CIs are absorbed in the innermost region of the star.

3.1.2 | Counterion Dynamics

The size of CIs, via the relation with the friction coefficient, is expected to affect the dynamical properties of the system, particularly their diffusivity. The latter, however, may also depend on structural characteristics of the PE (e.g., the number of arms f), as they modulate the strength of the electrostatic interactions and the amount of the excluded volume locally experienced by the CIs. To explore the possible interplay between all these factors, in Figure 4a we show the mean square displacement (MSD, see Equation (11)) across systems with varying number of arms and σ_{CI} values. First, we observe that CIs exhibit, on average, normal diffusion behavior, i.e., MSD $\propto Dt$. Diffusion coefficients, D, have been determined by linearly fitting the MSD curves and are reported in Figure S10. At fixed σ_{CI}, we observe that CI diffusivity decreases with increasing f, which can be rationalized assuming that the fraction of CIs confined within the star volume, $\langle\Phi\rangle$—which rises with the number of arms; see Figure 2b—is somewhat "slowed down" due to steric crowding. In contrast, the trends observed as a function of σ_{CI} with f held constant are less informative; the decrease in CI mobility with increasing size aligns with expectations, as larger ions experience greater friction coefficients.

Notwithstanding the previous observation, the strong inhomogeneity of electrostatic interactions between monomers and CIs, resulting from the star-shaped nature of the PE, suggests that the single averaged MSD curves may not provide enough information about the potential deviations of a fraction of the CIs from this average. Therefore, in Figures 4b–g and S8, we show the MSD curves for each individual CI trajectory from all independent runs. These curves reveal more complex behavior, especially in highly branched systems, with a fraction of CIs exhibiting MSD curves that deviate from normal diffusion trends at intermediate to long time scales ($t \gtrsim 10^2\tau_{LJ}$) when $f = 8$ and 15, clearly indicating anomalous behavior. Indeed, two distinct limiting behaviors can be identified: normal diffusion and subdiffusion. The proportion of the latter increases with both f and σ_{CI}, as evidenced by the distributions shown beside panels (b–e) and in Figure S9. The latter also provides a quantitative indication of the relative populations of CIs exhibiting the two behaviors. Indeed, we observe that at most 10% of the CIs are subdiffusive.

In other words, some CIs may be "slowed down" (which could even imply absorption or condensation) by the star for a much longer time than it typically takes for them to exhibit normal diffusive behavior. However, since all CIs are identical, the individual curves are expected to converge to the average MSD as $t \to \infty$. Thus, the presence of different behaviors highlights the ability of star-shaped PEs to trap CIs through absorption for a macroscopically limited amount of time, which depends on both the characteristics

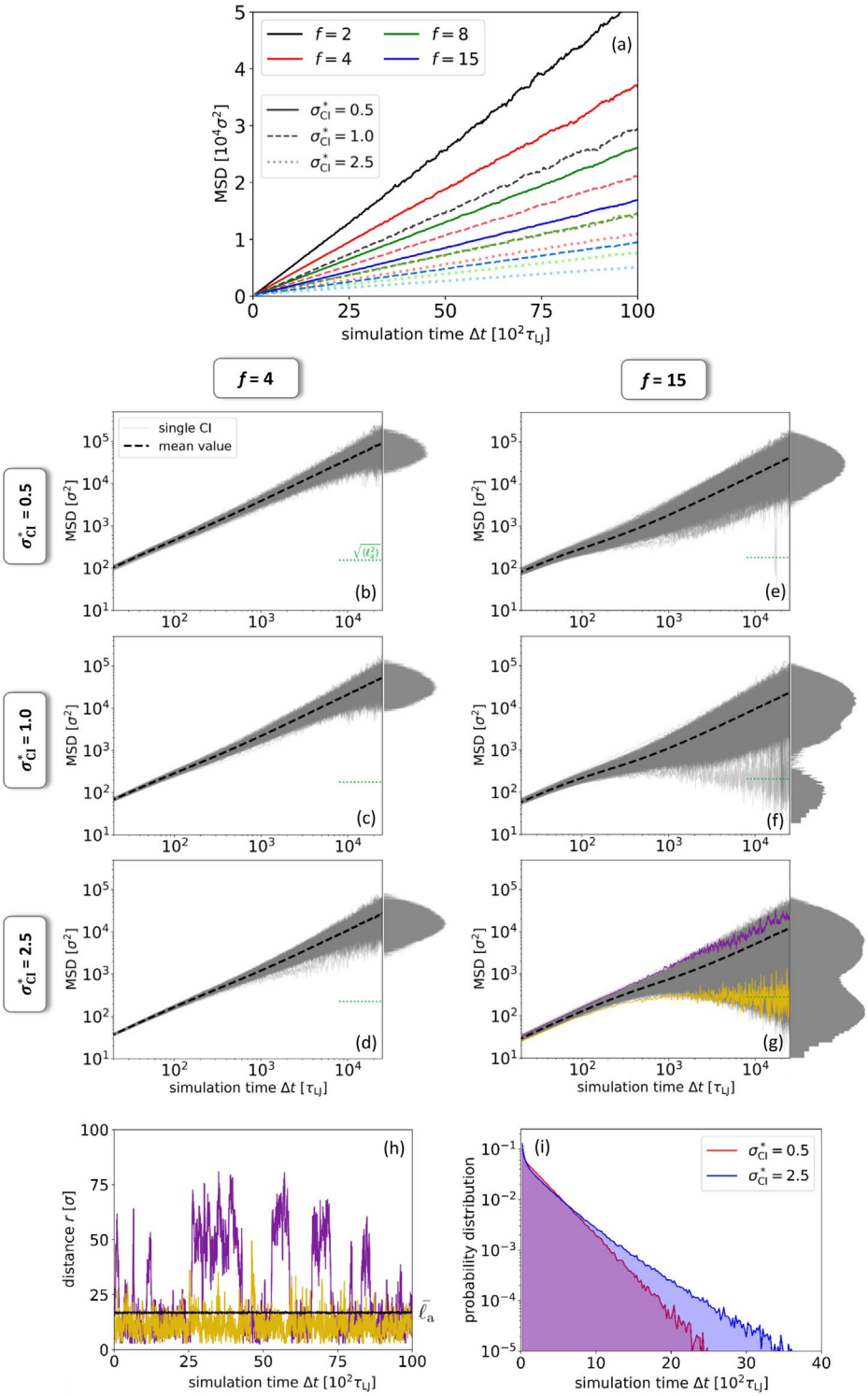

FIGURE 4 | (a) Averaged MSD of CIs for all the systems investigated. (b–g) MSD curves for individual CI trajectories for selected f and σ_{CI}—see Figure S8 for the remaining cases; the dashed black lines are average MSD curves, while the green dotted lines indicate the root mean square arm extension for comparison; next to each panel, we report the $\log_{10}$ of the MSD distributions computed in the range $10^4 \leq t/\tau_{LJ} \leq 2.5 \times 10^4$. (h) Time evolution of the distance between two selected CIs and the star center, with their MSD curves highlighted in panel (g); here, the black line represents the time evolution of the arm extension averaged across all chains. (i) Probability distribution of absorption lifetimes for $f = 15$ and CIs with $\sigma^*_{CI} = 0.5$ and 2.5.

of the PE (f) and the CIs (σ_{CI}). This heterogeneity in dynamics is also confirmed by the behavior of the non-Gaussian parameter α_2 [56, 57], which is reported and discussed in the SI, Figure S13.

Examples of these distinct behaviors for the case $f = 15$ and $\sigma^*_{CI} = 2.5$, which displays a strong bimodality in the MSD distribution, are highlighted in Figure 4g for two selected individual CI

trajectories and accompanied by the time evolution of their distance to the star center, r, which is shown in Figure 4h. The latter also includes the instantaneous value of the arm extension averaged across all the $f = 15$ arms, $\overline{\ell}_a$, as a function of time, which helps in determining whether the CIs are absorbed by the star. While it would be natural to hypothesize that in the case of normal diffusion, the CI remains desorbed and free to move in solution, we instead observe that it undergoes multiple absorption and desorption events throughout the simulation. Interestingly, even the CI exhibiting the subdiffusive behavior experiences rapid occurrences of desorption and re-absorption; however, it seldom reaches distances greater than 30σ (at which the reversible work to move a CI to the bulk is comparable to the thermal energy, see Figure 3h), and the time spent freely roaming outside the star PE appears very limited compared to a normally diffusing CI.

Before discussing further our results, it is important to note that the occurrence of multiple absorption and desorption events, even for the subdiffusive CIs, supports the adequacy of the duration of our simulations when it comes to sampling relatively rare events. Additionally, given our definition of absorption based on the *average* arm extension, $\overline{\ell}_a$, it is likely that a CI that has just crossed the threshold indicated in Figure 4h is still interacting, in a non-negligible way, with at least one arm of the PE, as their motion can be correlated. As a result, some of the events recorded as "desorptions" may be in fact false positives.

The most interesting, as somewhat unexpected, finding displayed in Figure 4 is the increase in population of subdiffusive CIs with σ_{CI}, a result contrasting with the idea that small CIs, accumulating in the inner star regions, may be the most likely to be "slowed down" by strong electrostatic interactions [18] and local monomer crowding. Indeed, simulations where the friction constant is set equal for all species regardless of their size (i.e., $\gamma^*_{\sigma_{CI}} = 1 \forall \sigma_{CI}$, as chosen in reference [18]) predict higher diffusivity for the larger species, see Figure S11.

Seeking for a rationalization of the observed increase of subdiffusing CIs with σ_{CI}, it is worth highlighting a few important details in the results of Figures 3 and 4:

i. CIs are progressively hindered by the populating the regions close to the star center surface upon increasing σ_{CI} primarily due to excluded volume effects (Figure 3c,d), so that the same regions have a higher effective charge density (hence, a higher effective charge, see Figure S14). In turn, implies that larger CIs would experience stronger inward pulling forces than smaller species, due to the centrally located uncompensated charge. As a result, the rate of exchange between the inner and middle regions of the PE should, on average, decrease as the size of the CIs increases.

ii. The structural rigidity (i.e., the relative positioning of monomers and the chain persistence length) of the PE arms in the inner regions seems to depend on the size of the CIs, as clearly shown in Figure S7c,d in the SI by the increased difference in relative heights of minima and maxima in the monomer radial distribution upon increasing σ_{CI}. This is particularly evident when $f = 8$ or 15, and for distances greater than 3σ, and it can be easily attributed to the reduced compensation of monomers charge above indicated, as well as the weaker tendency of bulky CIs to localize on the PE arms. Consequently, condensed bulky CIs condensed are likely to experience greater resistance during radial displacement due to the less uniform monomer charge density.

iii. The increasing effective charge in the core region with larger CIs creates a noticeable energy barrier, see Figure 3g,h. This effect can be partly attributed to the physical obstruction caused by the formation of a second shell of large CIs, which stratify due to electrostriction. This additional feature is expected to hinder the radial displacement of the CIs and, consequently, their exchange between the inner and more external regions. Although such exchanges remain possible (see Figure 4h), they are likely to occur via a unimolecular substitution mechanism, with the initial step involving the escape of a CI from the inner regions, as alternative pathways appear even slower. In fact, while the initiation of the exchange process through the entrance of a CI from more external zones is likely hindered by local crowding, it also seems highly improbable that collision energy would be transferred exclusively to a single CI lying in the inner region, effectively "kicking it out" in a bimolecular substitution-style mechanism. Importantly, the escape of a CI from the innermost PE regions would temporarily increase the effective charge of the latter by one unit, thereby intensifying the attraction with the remaining CIs.

Support for the idea that the rate of escape from inner regions depends on σ_{CI} is provided in Figure 4i, which depicts the probability distribution of the absorption lifetimes, τ_{abs}, for the case $f = 15$ and two CI sizes, $\sigma^*_{CI} = 0.5$ and 2.5. Here, it is possible to observe that the lifetime distribution for bulkier CIs exhibits a significantly more pronounced right tail compared to that of smaller CIs, indicating that a higher fraction of bulkier CIs remain absorbed for substantially longer periods and may consequently display subdiffusive behavior.

Another noticeable difference between the two distributions is observed at short time scales, where a larger population of short-lived ($\tau_{abs} \lesssim 150\tau_{LJ}$) absorption events is present for the bigger CIs. We attribute this to the fact that relatively more bulky CIs are residing at the periphery of the star (Figure 3c,d), which undergo a more facile and rapid desorption due to their reduced interaction with the PE. To further quantify the differences observed, we fitted the two time windows—i.e., (1) short times, $\tau_{abs} < 150\tau_{LJ}$, and (2) long times, $150\tau_{LJ} \leq \tau_{abs} \leq 2000\tau_{LJ}$—with exponential functions of the form $f(t) = Ae^{-t/\tau_{abs}} + B$. This yielded the following characteristic decay times: $\tau^{(1)}_{abs} \approx 35\tau_{LJ}$ and $\tau^{(2)}_{abs} \approx 279\tau_{LJ}$ for the smaller CIs; $\tau^{(1)}_{abs} \approx 28\tau_{LJ}$ and $\tau^{(2)}_{abs} \approx 320\tau_{LJ}$ for the bulkier ones.

3.2 | Star Polyelectrolytes Containing Differently Sized Counterions

To maximize the impact of mixing CIs with different sizes on the PE properties, and thus enhance the possibility of observing these effects, we selected systems containing two types of CIs with a substantial size difference: $\sigma^*_s = 0.5$ ("small") and $\sigma^*_B = 2.0$

("bulky"). We will investigate these systems as a function of the molar fractions of the smaller species, χ_s.

3.2.1 | Conformational and Thermodynamical Analysis

We begin by discussing the trajectory snapshots presented in Figure 5. We observe the following:

i. At fixed number of arms, f, the size of the PE decreases with increasing χ_s.

ii. The amount of small CIs condensed on the PE is generally higher than, or at least comparable to, the amount of bulky CIs, regardless of their molar fractions; this clearly suggests a preferential condensation of small CIs.

iii. Small CIs appear to localize in the innermost regions of the stars, i.e., close to the star center, a tendency that appears more pronounced as f increases.

To verify the observation done in item (i), Figures 6 and S15, respectively, report the root mean square arm extension, $\sqrt{\langle \ell_a^2 \rangle}$, and radius of gyration, $\sqrt{\langle R_g^2 \rangle}$, plotted against χ_s. Both conformational averages decrease as the fraction of small CIs increases. This can be explained by the fact that small CIs condense more on the PE arms, which reduces both the persistence length and the effective rigidity of the charged chains (see Figures 2 and 7, and the associated discussions).

In Figure 7a, we report the average fraction of *all* CIs condensed on the PE, $\langle \varphi \rangle$. The results indicate that $\langle \varphi \rangle$ increases with χ_s, reflecting the expected tendency for a greater condensation of the small CIs. Accordingly, $\langle \varphi_s \rangle$ and $\langle \varphi_B \rangle$, i.e., the fractions computed using the total number of CIs as the denominator (see Section 2.3.2 for exact definitions) increases and decreases respectively with χ_s, as illustrated in Figure S16.

More interesting is the behavior of $\langle \varphi_s^{(\chi)} \rangle$ and $\langle \varphi_B{}^{(\chi)} \rangle$, i.e., the fractions computed using, respectively, the number of small and bulky CIs as denominator (*de facto* representing effective partition coefficients). These results are shown in Figure 7b and reveal that both quantities decrease with χ_s. Importantly, the vast majority of small CIs are found condensed on the PE when their molar fraction is low, e.g., $\langle \varphi_s^{(\chi)} \rangle \approx 1$ for $f = 15$ and $\chi_s = 0.25$. This is likely due to the reduced well depth of the interaction curve between monomers and bulky CIs, which promotes preferential condensation/absorption of the smaller CIs. Additionally, the difficulty of bulky CIs in penetrating the innermost parts of the star, due to larger excluded volume effects, plays a role (*vide supra*), so that the smaller CIs are preferentially attracted and accumulated in these regions otherwise characterized by a high charge density (see Figure S14). This idea is clearly supported by the radial distribution functions in Figure 9 and the associated discussion.

We also notice that such an accumulation should, *de facto*, mitigate the strong intra- and inter-arm electrostatic repulsion near the star center due to correlation effects, which represent additional factor compensating the entropic disadvantage for the system associated to an increase in CI concentration in narrow volumes. The enthalpic aspects of the latter process should, however, become progressively less important (i.e., less negative) in determining the selective accumulation of a small CIs upon increasing χ_s due to the decrease of the charge density absolute values in the PE core (see Figure S17 for an estimate of the total system charge contained within a specific distance from the star center), which, in turn, would reduce the free energy gain of

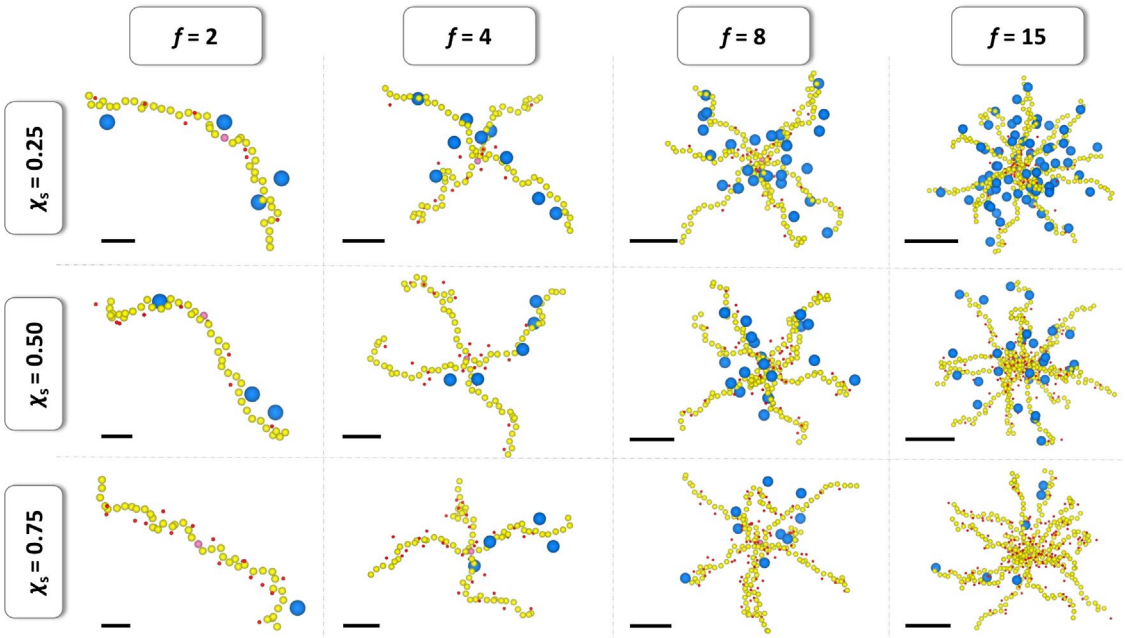

FIGURE 5 | Trajectory snapshots of star PEs with various numbers of arms and CI mixtures. Color scheme: Central monomer in pink, charged monomers in yellow, small CIs in red, bulky CIs in blue. For clarity, only *condensed* CIs are shown, and bonds between monomers are omitted to reduce visual clutter. As the conformations are not to scale, each snapshot includes a black bar proportional to the $\langle R_g^2 \rangle$ value to provide a sense of scale.

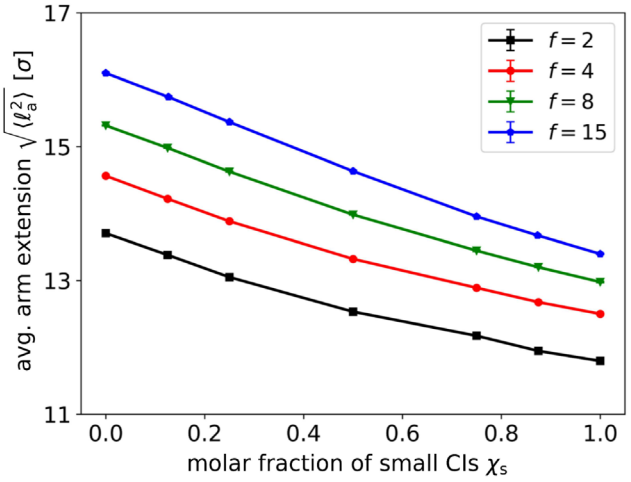

FIGURE 6 | Root mean squared arm extension as a function of the molar fraction of small CIs.

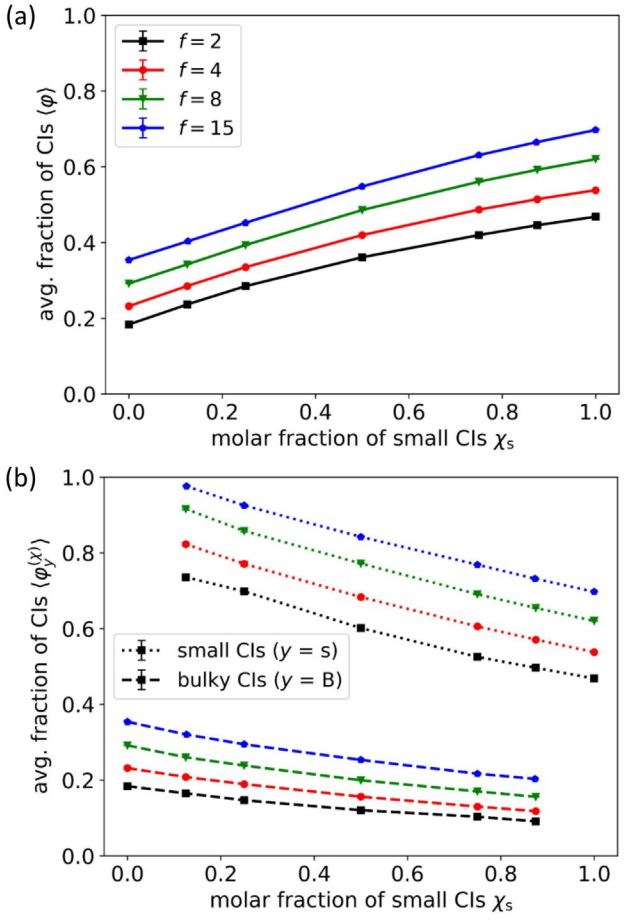

FIGURE 7 | Average fraction of condensed CIs computed by considering (a) all CIs together and (b) small and bulky CIs separately.

condensing/absorbing additional CIs even though these are available. This is indeed what shown in Figure 7b, where $\left\langle \varphi_s^{(\chi)} \right\rangle$ and $\left\langle \varphi_B{}^{(\chi)} \right\rangle$ are seen to deviate from the expected constant value as a function of χ_s that would be characteristic of partition coefficient

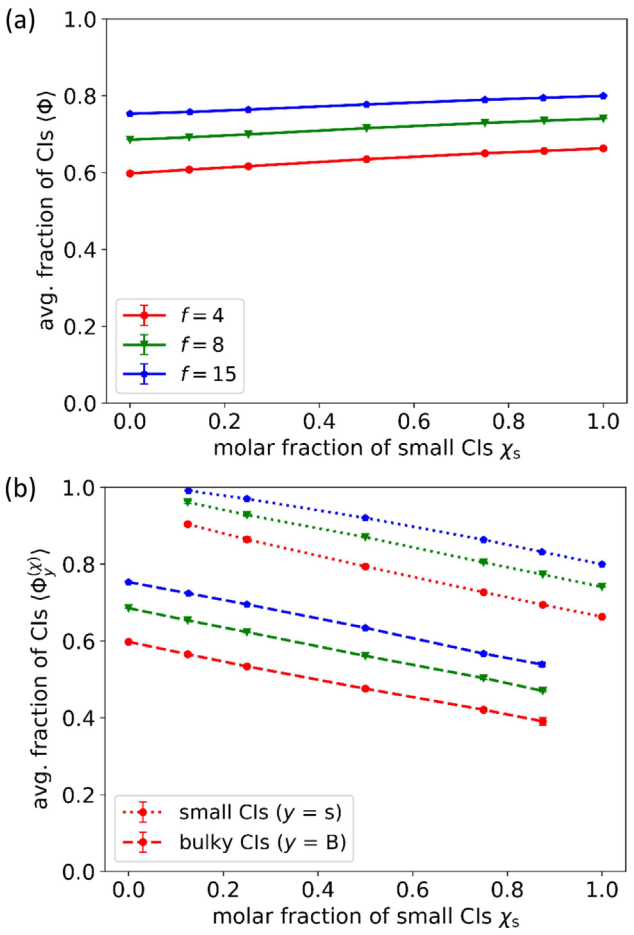

FIGURE 8 | Average fraction of absorbed CIs computed by considering (a) all CIs together and (b) small and bulky CIs separately.

independent of the species concentrations (i.e., with standard chemical potentials not affected by excluded volume and electrostatic interactions).

The trends observed for CI absorption exhibit qualitative similarities to the previously discussed data on CI condensation, as illustrated in Figure 8. In fact, $\langle \Phi \rangle$ increases with χ_s (Figure 8a), although at a lower rate compared to what is observed for CI condensation. This can be attributed to the fact that even a low fractions of small CIs may weaken the necessity of absorbing bulky CIs to neutralize (at least, partially) the core charge, as the latter species are not well suited due to their poor condensation and penetration ability (see Figure 2b, and also Figure S18 for a decomposition of the absorption of bulky and small CIs).

Similarly to what shown for CI condensation, the effective partition coefficients (i.e., $\left\langle \Phi_s^{(\chi)} \right\rangle$ and $\left\langle \Phi_B{}^{(\chi)} \right\rangle$) describing absorption of small and bulky CIs show decreasing values with χ_s (Figure 8b), a trend easily rationalized as done for $\left\langle \varphi_s^{(\chi)} \right\rangle$ and $\left\langle \varphi_B{}^{(\chi)} \right\rangle$.

As a consequence of what discussed, other quantities relevant for both the PE and solution are modified by χ_s. Thus, the effective charge of the PE, $\mathcal{Z}_{eff}$, decreases by about 15%–20% as χ_s increases from 0 to 1 (see Figure S20). A similar trend is also predicted for the osmotic coefficient, as the average virial pressure decreases with increasing χ_s, see Figure S21.

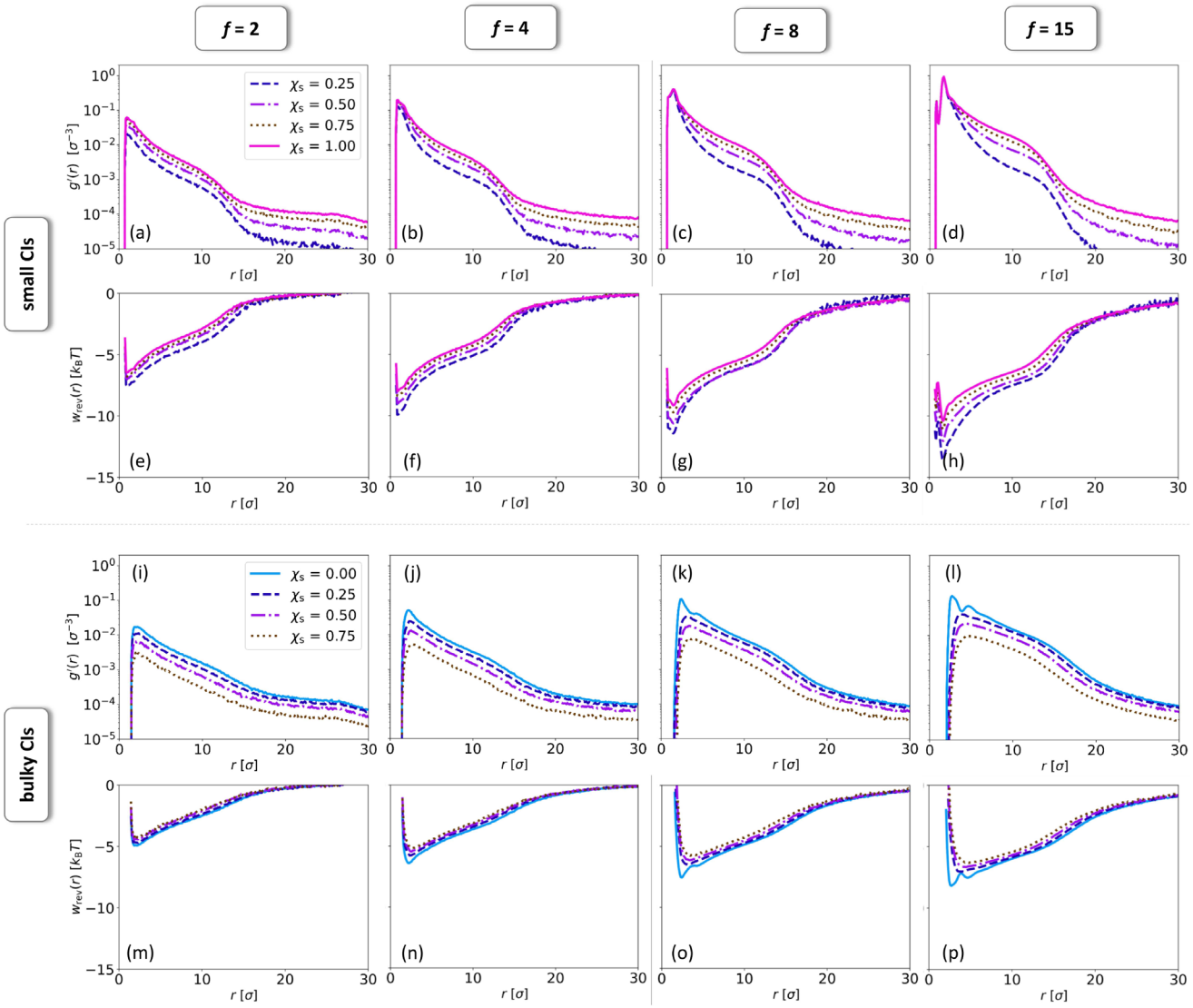

FIGURE 9 | Radial distribution functions of (a–d) small and (i–l) bulky CIs with respect to the star center, along with the reversible work required to move (e–h) a small CI or (m–p) a bulky CI from the bulk to a distance r from the star center.

To better comprehend the structural aspects of mixed CIs condensation and absorption, the radial distribution functions for the two species are shown in Figure 9. Focusing first on the small CIs, the results confirm their preferential localization in the innermost regions of the star, with their $g'(r)$ exhibiting a marked peak very close to the center. Interestingly, while for the $f = 2$ and 4 systems the probability densities at short distances increase with χ_s due to mere mass effect, when $f = 8$ and 15 the distributions overlap for $r \lesssim 3$, indicating that the system is capable of saturating the first absorption shells around the star center even when the concentration of small CIs is very low. Moreover, the noticeable absence of marked tails at $r \gtrsim \sqrt{\langle \ell_a^2 \rangle}$ for distributions where $\chi_s \leq 0.50$ and $f \geq 8$ confirms that, under these conditions, the vast majority of small CIs are not free in solution but are instead absorbed into the PE. Aside from the obvious decrease in magnitude as χ_s increases, we also observe for the bulky CIs that the main peak gradually shifts to higher distances, while the secondary peak disappears as χ_s increases when $f = 8$ and 15. This suggests that in highly branched stars bulky CIs migrate farther from the star center as they are progressively replaced by smaller CIs.

Figure 9e–h,m–p illustrates the reversible work required to displace small and bulky CIs from the innermost region of the star, i.e., $-w_{rev}(r = r_1)$ (where r_1 corresponds to the position of the main peak in $g'(r)$), showing its dependency on χ_s. We observe that the $w_{rev}(r)$ curves for bulky CIs are only mildly affected by the progressive substitution with small ions, the energy required to desorb them increasing only slightly with χ_s. In fact, the largest change of $w_{rev}(r = r_1)$ for bulky CIs is a reduction by only $\sim 2k_BT$ (i.e., approximately 1.2 kcal/mol) when χ_s changes from 0 to 0.75 and $f = 15$. Composition has, instead, a somewhat stronger impact on the energetics involving small CIs: in this case, $-w_{rev}(r = r_1)$ decreases by about one k_BT unit (0.6 kcal/mol) for the linear PE, and by up to $\sim 3k_BT = 1.8$ kcal/mol when $f = 15$.

Overall, our results demonstrate that in the presence of a binary mixture of differently sized CIs, star PEs tend to preferentially interact with the smaller species. This tendency becomes more

pronounced as the number of arms increases and as the molar fraction of the smaller CIs decreases, and it could be more effectively evaluated in terms of the selectivity, $S_s^{(y)}$, of the PE toward the condensation ($y = \varphi$, solid lines) and absorption ($y = \Phi$, dashed lines) of small CIs (see Section 2.3.3 and Equations (9) and (10) for a definition). From the results shown in Figure 10, we observe that:

i. $S_s^{(\varphi)}$ and $S_s^{(\Phi)}$ are consistently greater than 1, regardless the number of arms and the mixture composition, thus confirming that the preferential interaction of the PE with the smaller CIs is a general phenomenon.

ii. At fixed f and χ_s, $S_s^{(\varphi)} > S_s^{(\Phi)}$; this expected, as CI absorption is less influenced by their sizes compared to CI condensation (Figures 2b, 7, and 8).

iii. At fixed χ_s, selectivity monotonically increases with the number of arms; however, the lower the molar fraction of small CIs, the stronger the preferential selectivity toward them.

Thus, as a takeaway message, to maximize selectivity toward smaller CIs, the PEs should be highly branched and operate at low molar fractions of the target species.

3.2.2 | Counterion Dynamics

Given the marked interplay between CI molar fractions, χ_s and χ_B, and diameters, σ_s and σ_B, in defining the spatial distribution of both species, one may wonder whether the dynamical properties of the latter could be impacted as well. To investigate this possibility, Figure 11a,b shows the averaged MSD curves for small and bulky CIs, respectively. From these, we observe, first, that the MSD of both species decreases as the number of arms increases at a chosen χ_s, a finding expected basing on the MSD versus CI size reported in Figure 4. Second, we note that the mixture composition has a much greater impact on the difference in mobility of small CIs compared to bulky ones, a result most conveniently seen by examining the diffusion coefficients reported in Figure S25. From these data, it also emerges that small CIs are not always "better diffusers" than the bulkier counterparts despite the difference the experienced friction, as one might have suggested basing on the results on "pure" CIs in reported in Figure S10. In fact, the highly branched PEs appear to reduce small CIs diffusivity below the one of the bulky species, at least for $\chi_s \leq 0.5$.

To understand the root cause of this unexpected finding, Figure 11c–f reports the MSD curves for all the CIs across all the simulation trajectories. In the following, we shall however limit ourselves to discuss only results for $f = 8$ and 15, as less branched PEs conform with the expected behavior of presenting higher MSD for smaller CIs, the difference with the bulkier counterparts being further increased by increasing χ_s as a larger fraction of small CIs are not condensed.

For stars with 15 (and 8, see Figure S22) arms, the difference in diffusivity between the two ionic species becomes much more pronounced. At $\chi_s = 0.25$, we observe that smaller CIs exhibit lower mobility than bulky ones over both short and long time scales. Additionally, the MSD curves of individual CIs of both species, tend to split into two distinct groups: some ions exhibit normal diffusion, while others display subdiffusive behavior (see also Figure S23). For the smaller species, subdiffusive ions are a conspicuous fraction of the small CIs (nearly 30%), whereas normal diffusing ions are the vast majority for the bulky species (above 95%). The bimodal nature of the MSD distributions is particularly evident in the values presented alongside the panels for both species and in Figure S23. As χ_s increases, the population of subdiffusive CIs of both species decreases. Indeed, the low MSD peak vanishes completely for bulky CIs at $\chi_s = 0.75$; a few subdiffusive small CIs, instead, persist in the same conditions. This strong heterogeneity in dynamics is also reflected in the behavior of the non-Gaussian parameter α_2 [56, 57], as reported in Figure S26.

The complex dynamics just described for highly branched stars can be explained as follows:

i. At low χ_s values, the vast majority (i.e., 90%) of small CIs is absorbed in the innermost regions of the star (see Figures 8 and 9d), and the dynamic exchange between PE and solution is scarce, which explains the high fraction of subdiffusive small CIs. Interestingly, the number of CIs present likely does not saturate the PE. In fact, a significant fraction of the bulky CIs (∼ 75%, see Figure 8) is absorbed as well, with the innermost being located close to the tallest peak of the small CIs. Apart from leading to the slowing down of a fraction of large CIs, as clearly evidenced by the marked bimodality in their MSD distributions, the large ions located closer to the PE core may also force the small CIs dwelling closer to the center to follow a more tortuous path during their migration toward the external PE regions, *de facto* reducing the rate of exchange and diffusivity.

ii. As χ_s increases, the dynamic exchange of small CIs between the PE and the solution becomes progressively more facile, as more of these ions are available in peripheral

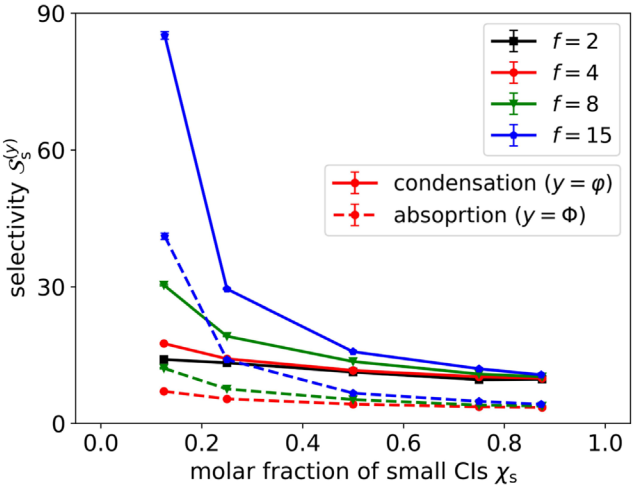

FIGURE 10 | Selectivity toward the condensation (solid lines) and absorption (dashed lines) of small CIs, shown as a function of χ_s and for systems with varying numbers of arms.

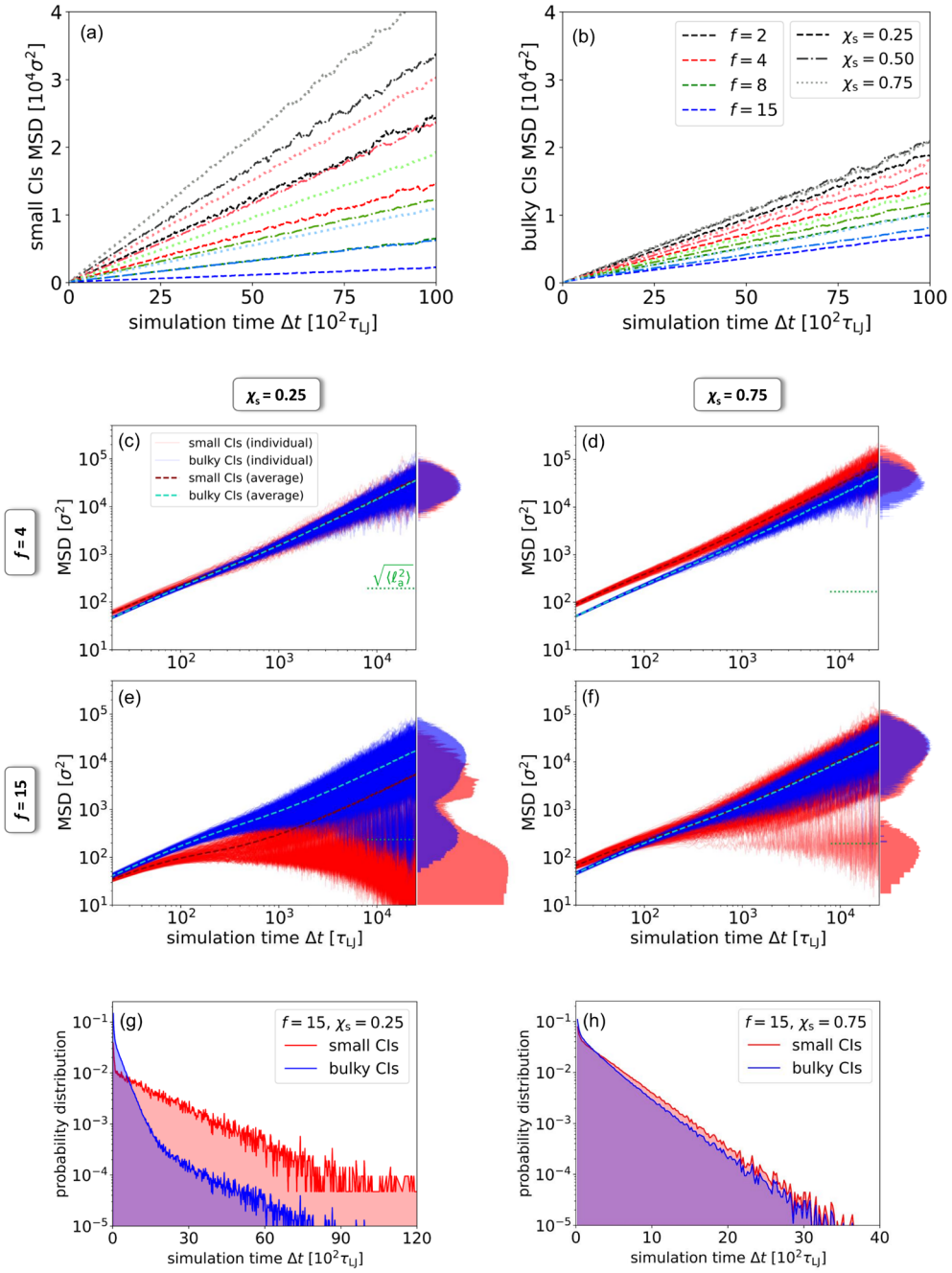

FIGURE 11 | (a, b) Average MSD of, respectively, small and bulky CIs for systems with various numbers of arms and CIs compositions. (c–f) MSD curves for each individual CI trajectory in selected systems with varying f and σ_{CI}—see Figures S22 and S23 for additional cases; the dashed light-blue and dark-red lines are average MSD curves, while the green dotted lines indicate the root mean square arm extension for comparison; beside each panel, we report the $\log_{10}$ of the MSD distributions computed for the time range $10^4 \geq t / \tau_{LJ} \geq 2.5 \times 10^4 \tau_{LJ}$. (g, h) Probability distribution of absorption lifetimes for 15-arms star and $\chi_s = 0.25$ and 0.75, respectively.

zones. This lead to a reduction in the number of small CIs that remain absorbed for extended periods, thereby increasing their average diffusion. Similarly, the population of subdiffusive bulky CIs decreases, as they are no longer required to neutralize the core charge and progressively desorb with increasing χ_s.

That the peculiar trend in the fraction of subdiffusive CIs may be explained by the different ions exchange rates between the PE and the solution as a function of the mixture composition is well supported by the results shown in Figure 11g,h, which provides the probability distributions of the absorption lifetimes, τ_{abs}, for both small and bulky CIs at $f = 15$ and for two mixture compositions, $\chi_s = 0.25$ and 0.75.

At high molar fractions of small CIs, the distributions for the two groups appear quantitatively similar, with the smaller ions exhibiting a slightly more pronounced right tail. This latter aspect well correlates with the large fraction of small CIs located in the internal regions of the star PE compared to that of bulkier CIs, with the former requiring a long time to diffuse through the tortuous paths imposed by the large CIs (*vide supra*), whereas

it is more likely for the latter to gather enough energy to escape beyond the PE arms length. The same concept also explains the higher frequency of short-lived absorption events observed for bulky CIs, which appear nontatistical in nature and indicate a higher concentration of such species close to the absorption boundary compared to the smaller counterparts.

A fitting of short ($\tau_{abs} < 150\tau_{LJ}$) and intermediate-long timescales ($150\tau_{LJ} \leq \tau_{abs} < 2000\tau_{LJ}$), akin to the regression performed for the data presented in Figure 4i, yields, $\tau_{abs}^{(1)} \approx 31\tau_{LJ}$ and $\tau_{abs}^{(2)} \approx 405\tau_{LJ}$ for the small CIs, and $\tau_{abs}^{(1)} \approx 27\tau_{LJ}$ and $\tau_{abs}^{(2)} \approx 319\tau_{LJ}$ for the bigger ones. Comparing these results with those obtained in the presence of only one type of CIs (i.e., for $\chi_s = 0$ and 1; see Figure S12), we observe that, while the absorption lifetime of bulky CIs seems to not be significantly affected by χ_s, the absorption lifetime of small CIs dramatically increases when mixed with bulkier species due to the effects mentioned above.

The results at $\chi_s = 0.25$ are even more striking and provide further support for the mechanisms discussed earlier. For the bulky CIs, we observe that three exponential functions are required to fully represent the lifetime distribution. The fits yield $\tau_{abs}^{(2)} = 325\tau_{LJ}$ and $\tau_{abs}^{(3)} = 1160\tau_{LJ}$ (the latter corresponding to the range $2000\tau_{LJ} \leq \tau_{abs} \leq 6000\tau_{LJ}$). While the former is nearly identical to the $\chi_s = 0$ and $\chi_s = 0.75$ cases, and thus corresponds to the desorption time typical of the bulky CIs, the second is a direct consequences of their subdiffusive fraction, which requires a longer time to reach the threshold as more internally adsorbed. The lifetime distribution appears even more complex for the small CIs, presenting an extremely longer decay time (for $150\tau_{LJ} \leq \tau_{abs} < 8000\tau_{LJ}$, $\tau_{abs}^{(2)} = 1685\tau_{LJ}$; i.e., a sixfold increase) compared to the case $\chi_s = 1$, and a nearly flat component when $\tau_{abs} > 8000\tau_{LJ}$. The latter feature suggests that the mechanism leading to the desorption of the CIs dwelling closer to the star center than the layer formed by innermost absorbed bulky CIs is saturated, and aligns with the expectation that such process is governed by the opening and closing of pathways for escaping through electrostatically repelling species.

To conclude, it is important to emphasize that simulations using a uniform friction coefficient lead to inaccurate results, see Figure S24. Specifically, setting $\gamma^* = 1$ for all species overestimates the mobility of bulky CIs and underestimates that of smaller ones. This inflates the population of subdiffusive small CIs while reducing that of subdiffusive bulky ones, including those that would hinder the escape of small CIs from the core regions. Nevertheless, the overall qualitative trend of a decreasing population of subdiffusive CIs with increasing χ_s is still captured.

4 | Conclusions

Motivated by previous computational [16, 18, 19, 21–23, 29, 30, 37] and experimental [26–28] studies evidencing their importance in the solution properties of PEs, we systematically investigated the impact of counterion (CI) size on the behavior of star-shaped polyelectrolytes (PEs) in dilute aqueous solutions by means of Langevin simulations and a primitive model of electrolytes.

With the aim to gain a few fundamental physical insights, we thus simulated star-shaped PEs with different arm numbers, $f \in \{2,4,8,15\}$, in the presence of CIs of various diameters, $\sigma_{CI} \in [0.5\sigma, 2.5\sigma]$. We found that CI size significantly affects PE conformations, with both the radius of gyration and arm extension increasing with σ_{CI} (Figure 2a). Such behavior can be attributed to the reduced well depth of the interaction between the charged monomers and the larger CIs, as noted in prior studies [18, 37]. Thus, the effective inter- and intra-arm interactions strengthen, leading to chains linearization, as σ_{CI} increases (Figure 2b). The reduction in the monomers–CIs electrostatic interaction leads also to a decrease in the fractional amount of condensed or absorbed CIs upon increasing σ_{CI}. The latter quantity, however, appears much less affected, indicating that bulkier CIs partially detach from the charged chains but remain within the volume defined by the star arms. We showed that these phenomena directly impact solution properties such as the osmotic coefficient [51].

As for the ionic transport, we evidenced that small CIs show higher diffusivity than bulky ones due to the lower friction they experience despite their strong electrostatic attraction with the charged arms and their remarkably high ability to penetrate the innermost regions of highly branched stars (Figure 4). This result directly stems from considering an "à la Stokes" size-dependent friction coefficient that was missing in previous studies [16, 18], where uniform friction was assumed for all particles. Interestingly, a fraction of CIs was found to exhibit subdiffusive behavior in highly branched stars within the time scales explored by our simulations, with the population of subdiffusing CIs growing from almost absent to able of impacting average properties upon increasing σ_{CI}. We demonstrated that this trend is related to a reduction in CIs dynamic exchange between PE and solution as their size increases.

Hinging on the information regarding PEs in the presence of homogeneously-sized, we then investigated how the overall behavior of the latter is modified when in the presence of a mixture of two differently sized CIs, namely "small" ($\sigma_s = 0.5\sigma$) and "bulky" ($\sigma_B = 2.0\sigma$), varying both the number of arms, f, and the molar fraction of the smaller species, χ_s. We found that while the PE size decreases with χ_s (Figure 6), both the fraction of condensed and absorbed CIs increase with it (Figures 7 and 8). These changes were expected basing on the trends seen for single-size CI PEs. Interestingly, a core–shell-like structure is formed in the presence of CIs with different diameters, with the smaller ions occupying the innermost region of the star, and the bulky ones positioning themselves in the outer shells (Figure 9). To quantify the preferential accumulation of specific species, we calculated the selectivity toward condensation and absorption of small CIs and showed that both increase with f and decrease with χ_s. This demonstrates that highly branched PE may act as better selective sievers for small CIs, especially under conditions of scarcity of the latter (Figure 10).

Notably, the accumulation of the smaller species near the core of our highly branched stars is more pronounced than that observed by Kłos and Paturej in charged dendrimers under aqueous solution conditions [22]. This difference may partly stem from the varying density profiles of charged monomers in the two PE architectures; however, the smaller size disparity between the CIs in their

mixture ($\sigma_s = \sigma$ and $\sigma_B = 2\sigma$) likely contributed to reducing the absorption disparity. Regarding dendrimers, it would be interesting to investigate the so called "hollow-core dendrimers" [58–60] (i.e., dendrimers with low monomer density near the core) in the presence of mixtures of differently sized CIs, as such systems might exhibit an "inverted" core–shell structure, where the bulkier species preferentially accumulate in the innermost regions.

Finally, we investigated the dynamics of the two CI species in the binary mixture, revealing that their diffusivity is strongly influenced by their co-presence in unexpected ways. Interestingly, the small CIs exhibited pronounced subdiffusion, with the fraction of such species involved decreasing as σ_{CI} increased (Figure 11). A similar trend was observed for the bulky CIs, suggesting that a higher fraction of small CIs facilitates the larger counterparts in escaping from the inner regions of the star, where they would otherwise be trapped by the uncompensated core charge. Nonetheless, bulky CIs are not entirely released from the PE core regions when χ_s is low, and their presence restricts the ability of small CIs to escape, due to both excluded volume effects and electrostatic repulsion. This behavior was, once again, rationalized by analyzing the distribution of absorption lifetimes, which reveals that small CIs tend to remain absorbed for extended periods when χ_s is low.

A natural extension of our investigation would be to explore how CI sizes and mixtures affect the properties of PE brushes [39–41]. If preferential size selectivity was observed, it would be intriguing to investigate how this selectivity could be fine-tuned by varying the grafting density and the curvature of the substrate. Relevant implications for ionic exchange chromatography should be provided from such a study. Size-selective water desalination mediated by PE hydrogels compression [61–65] may also be a target for a similar exploration, varying charge and network architecture. Investigations are currently underway to explore these aspects.

Acknowledgments

A.T. acknowledges post-doctoral fellowships from Università degli Studi dell'Insubria (assegno di ricerca junior, 2022). M.M. acknowledges funding from Università degli Studi dell'Insubria (Fondo d'Ateneo per la Ricerca, FAR2023).

References

1. J. Yu, J. Mao, G. Yuan, et al., "Structure of Polyelectrolyte Brushes in the Presence of Multivalent Counterions," *Macromolecules* 49 (2016): 5609–5617.

2. C. G. Lopez, F. Horkay, R. Schweins, and W. Richtering, "Solution Properties of Polyelectrolytes With Divalent Counterions," *Macromolecules* 54 (2021): 10583–10593.

3. F. Carnal and S. Stoll, "Chain Stiffness, Salt Valency, and Concentration Influences on Titration Curves of Polyelectrolytes: Monte Carlo Simulations," *Journal of Chemical Physics* 134 (2011): 044909.

4. A. Jusufi, O. Borisov, and M. Ballauff, "Structure Formation in Polyelectrolytes Induced by Multivalent Ions," *Polymer* 54, no. 8 (2013): 2028–2035. Special issue in honor of Axel H.E. Müller.

5. A. Chremos and J. F. Douglas, "Influence of Higher Valent Ions on Flexible Polyelectrolyte Stiffness and Counter-Ion Distribution," *Journal of Chemical Physics* 144 (2016): 164904.

6. R. Staňo, L. Nová, F. Uhlík, and P. Košovan, "Multivalent Counterions Accumulate in Star-Like Polyelectrolytes and Collapse the Polymer in Spite of Increasing Its Ionization," *Soft Matter* 16 (2020): 1047–1055.

7. A. Tagliabue, L. Izzo, and M. Mella, "Interface Counterion Localization Induces a Switch Between Tight and Loose Configurations of Knotted Weak Polyacid Rings Despite Intermonomer Coulomb Repulsions," *Journal of Physical Chemistry B* 124 (2020): 2930–2937.

8. M. Jacobs, C. G. Lopez, and A. V. Dobrynin, "Quantifying the Effect of Multivalent Ions in Polyelectrolyte Solutions," *Macromolecules* 54 (2021): 9577–9586.

9. A. Tagliabue, C. Micheletti, and M. Mella, "Tuning Knotted Copolyelectrolyte Conformations via Solution Properties," *Macromolecules* 55 (2022): 10761–10772.

10. A. Tagliabue, J. Landsgesell, M. Mella, and C. Holm, "Can Oppositely Charged Polyelectrolyte Stars Form a Gel? A Simulational Study," *Soft Matter* 17 (2021): 1574–1588.

11. R. Staňo, P. Košovan, A. Tagliabue, and C. Holm, "Electrostatically Cross-Linked Reversible Gels—Effects of pH and Ionic Strength," *Macromolecules* 54 (2021): 4769–4781.

12. C. E. Sing and S. L. Perry, "Recent Progress in the Science of Complex Coacervation," *Soft Matter* 16 (2020): 2885–2914.

13. S. P. Moulik, A. K. Rakshit, A. Pan, and B. Naskar, "An Overview of Coacervates: The Special Disperse State of Amphiphilic and Polymeric Materials in Solution," *Colloids and Interfaces* 6 (2022): 45.

14. M. Mella and A. Tagliabue, "Impact of Chemically Specific Interactions Between Anions and Weak Polyacids on Chain Ionization, Conformations, and Solution Energetics," *Macromolecules* 55 (2022): 4533–4547.

15. R. Fernandez-Alvarez, L. Nová, F. Uhílk, et al., "Interactions of Star-Like Polyelectrolyte Micelles With Hydrophobic Counterions," *Journal of Colloid and Interface Science* 546 (2019): e371–e380.

16. A. A. Gavrilov, A. V. Chertovich, and E. Y. Kramarenko, "Conformational Behavior of a Single Polyelectrolyte Chain With Bulky Counterions," *Macromolecules* 49 (2016): 1103–1110.

17. A. M. Tom, S. Vemparala, R. Rajesh, and N. V. Brilliantov, "Regimes of Electrostatic Collapse of a Highly Charged Polyelectrolyte in a Poor Solvent," *Soft Matter* 13 (2017): 1862–1872.

18. Y. D. Gordievskaya, A. A. Gavrilov, and E. Y. Kramarenko, "Effect of Counterion Excluded Volume on the Conformational Behavior of Polyelectrolyte Chains," *Soft Matter* 14 (2018): 1474–1481.

19. Y. D. Gordievskaya and E. Y. Kramarenko, "Effect of Counterion Size on the Structure of a Flexible Polyelectrolyte Chain in Low-Polar Solvents," *Polymer Science, Series C* 60 (2018): 37–48.

20. Y. D. Gordievskaya, Y. A. Budkov, and E. Y. Kramarenko, "An Interplay of Electrostatic and Excluded Volume Interactions in the Conformational Behavior of a Dipolar Chain: Theory and Computer Simulations," *Soft Matter* 14 (2018): 3232–3235.

21. J. S. Kłos and J. Paturej, "Charged Dendrimers With Finite-Size Counterions," *Journal of Physical Chemistry B* 124 (2020): 7957–7968.

22. J. S. Kłos and J. Paturej, "Spatial Segregation of Mixed-Sized Counterions in Dendritic Polyelectrolytes," *Scientific Reports* 11 (2021): 8108.

23. T. H. Pial, H. S. Sachar, and S. Das, "Quantification of Mono- and Multivalent Counterion-Mediated Bridging in Polyelectrolyte Brushes," *Macromolecules* 54 (2021): 4154–4163.

24. N. B. Wyatt and M. W. Liberatore, "The Effect of Counterion Size and Valency on the Increase in Viscosity in Polyelectrolyte Solutions," *Soft Matter* 6 (2010): 3346–3352.

25. Y. Nishiyama and M. Satoh, "Solvent- and Counterion-Specific Swelling Behavior of Poly(Acrylic Acid) Gels," *Journal of Polymer Science Part B: Polymer Physics* 38 (2000): 2791–2800.

26. O. E. Philippova, A. M. Rumyantsev, E. Y. Kramarenko, and A. R. Khokhlov, "New Type of Swelling Behavior Upon Gel Ionization: Theory vs Experiment," *Macromolecules* 46 (2013): 9359–9367.

27. H. Mori, M. Wakagawa, S. Kuroki, and M. Satoh, "Counterion Mixing Effects on Conformational Transitions of Polyelectrolytes 3: Coil-Globule Transition of Alkali Metal and Tetraalkyl Ammonium Polysulfonates," *Colloid and Polymer Science* 293 (2015): 1023–1033.

28. A. M. Rumyantsev, A. Pan, S. Ghosh Roy, P. De, and E. Y. Kramarenko, "Polyelectrolyte Gel Swelling and Conductivity vs Counterion Type, Cross-Linking Density, and Solvent Polarity," *Macromolecules* 49 (2016): 6630–6643.

29. J. Jiang, X. Chen, S. Yang, and E. Chen, "The Size and Affinity Effect of Counterions on Self-Assembly of Charged Block Copolymers," *Journal of Chemical Physics* 152, no. 12 (2020): 124901.

30. A. Gavrilov, "Effect of the Counterion Size on Microphase Separation in Charged-Neutral Diblock Copolymers," *Journal of Chemical Physics* 158 (2023): 054901.

31. D. Rau and V. Parsegian, "Direct Measurement of the Intermolecular Forces Between Counterion-Condensed DNA Double Helices. Evidence for Long Range Attractive Hydration Forces," *Biophysical Journal* 61, no. 1 (1992): 246–259.

32. T. T. Nguyen, "Grand-Canonical Simulation of DNA Condensation With Two Salts, Effect of Divalent Counterion Size," *Journal of Chemical Physics* 144, no. 6 (2016): 065102.

33. K. Wang, Y.-X. Yu, G.-H. Gao, and G.-S. Luo, "Preferential Interaction Between DNA and Small Ions in Mixed-Size Counterion Systems: Monte Carlo Simulation and Density Functional Study," *Journal of Chemical Physics* 126 (2007): 135102.

34. A. Savelyev and G. A. Papoian, "Electrostatic, Steric, and Hydration Interactions Favor Na+Condensation Around DNA Compared With K+," *Journal of the American Chemical Society* 128 (2006): 14506–14518.

35. M. Gebala, S. Bonilla, N. Bisaria, and D. Herschlag, "Does Cation Size Affect Occupancy and Electrostatic Screening of the Nucleic Acid Ion Atmosphere?," *Journal of the American Chemical Society* 138 (2016): 10925–10934.

36. C. Plesa, D. Verschueren, S. Pud, et al., "Direct Observation of DNA Knots Using a Solid-State Nanopore," *Nature Nanotechnology* 11 (2016): 1093–1097.

37. A. Tagliabue, C. Micheletti, and M. Mella, "Effect of Counterion Size on Knotted Polyelectrolyte Conformations," *Journal of Physical Chemistry B* 128 (2024): 4183–4194.

38. S. Ghosh and A. Kundagrami, "Effect of Counterion Size on Polyelectrolyte Conformations and Thermodynamics," *Journal of Chemical Physics* 160 (2024): 084909.

39. H.-G. Tan, L.-D. Guo, H.-Y. Qian, L.-X. Liu, Q.-H. Hao, and B. Miao, "Size Effect of Multivalent Counterions on Polyelectrolyte Brushes in Different Polar Solvents," *Macromolecules* 56 (2023): 9312–9323.

40. D. Prusty, A. Gallegos, and J. Wu, "Modeling Ionic and Sequence Effects on the Swelling Behavior of Polyampholyte Brushes," *Macromolecules* 57 (2024): 6666–6680.

41. R. Ishraaq and S. Das, "All-Atom Molecular Dynamics Simulations of Cationic Polyelectrolyte Brushes in the Presence of Halide Counterions," *Macromolecules* 57 (2024): 3037–3046.

42. A. Aliakseyeu, E. Truong, Y.-Y. Hu, R. Sayko, A. V. Dobrynin, and S. A. Sukhishvili, "Self-Diffusion of Star and Linear Polyelectrolytes in Salt-Free and Salt Solutions," *Macromolecules* 58 (2025): 240–248.

43. A. Gulati and C. G. Lopez, "Viscosity of Polyelectrolytes: Influence of Counterion and Solvent Type," *ACS Macro Letters* 13 (2024): 1079–1083.

44. H. Landfield, N. Kalamaris, and M. Wang, "Extreme Dependence of Dynamics on Concentration in Highly Crowded Polyelectrolyte Solutions," *Science Advances* 10 (2024): eado4976.

45. K. Kremer and G. S. Grest, "Dynamics of Entangled Linear Polymer Melts: A Molecular-Dynamics Simulation," *Journal of Chemical Physics* 92 (1990): 5057–5086.

46. J. D. Weeks, D. Chandler, and H. C. Andersen, "Role of Repulsive Forces in Determining the Equilibrium Structure of Simple Liquids," *Journal of Chemical Physics* 54 (1971): 5237–5247.

47. Q. Liao, J.-M. Y. Carrillo, A. V. Dobrynin, and M. Rubinstein, "Rouse Dynamics of Polyelectrolyte Solutions: Molecular Dynamics Study," *Macromolecules* 40 (2007): 7671–7679.

48. P. Polezhaev, T. Belloň, N. C. Kurospajeva, L. Vobecká, and Z. Slouka, "Molecular Sieving of Tetraalkylammonium Cations on Cation Exchange Systems in DC Electric Field," *Separation and Purification Technology* 241 (2020): 116691.

49. F. Weik, R. Weeber, K. Szuttor, et al., "ESPResSo 4.0 – An Extensible Software Package for Simulating Soft Matter Systems," *European Physical Journal Special Topics* 227 (2019): 1789–1816.

50. M. Rahimi, J. K. Singh, and F. Müller-Plathe, "Adsorption and Separation of Binary and Ternary Mixtures of SO_2, CO_2, and N_2 by Ordered Carbon Nanotube Arrays: Grand-Canonical Monte Carlo Simulations," *Physical Chemistry Chemical Physics* 18 (2016): 4112–4120.

51. O. V. Borisov, E. B. Zhulina, F. A. M. Leermakers, M. Ballauff, and A. H. E. Müller, *Self Organized Nanostructures of Amphiphilic Block Copolymers I*, ed. A. H. E. Müller and O. Borisov (Springer, 2011), 1–55.

52. M. Ullner, K. Qamhieh, and B. Cabane, "Osmotic Pressure in Polyelectrolyte Solutions: Cell-Model and Bulk Simulations," *Soft Matter* 14 (2018): 5832–5846.

53. https://espressomd.github.io/doc/analysis.html#pressure.

54. U. Essmann, L. Perera, M. L. Berkowitz, T. Darden, H. Lee, and L. G. Pedersen, "A Smooth Particle Mesh Ewald Method," *Journal of Chemical Physics* 103 (1995): 8577–8593.

55. J. G. Kirkwood, "Statistical Mechanics of Fluid Mixtures," *Journal of Chemical Physics* 3 (1935): 300–313.

56. A. Rahman, "Correlations in the Motion of Atoms in Liquid Argon," *Physical Review* 136 (1964): A405–A411.

57. D. Sil, E. Osmanbasic, S. C. Mandal, A. Acharya, and C. Dutta, "Variable Non-Gaussian Transport of Nanoplastic on Supported Lipid Bilayers in Saline Conditions," *Journal of Physical Chemistry Letters* 15 (2024): 5428–5435.

58. P. de Gennes and H. Hervet, "Statistics of Starburst Polymers," *Journal de Physique Lettres* 44 (1983): 351–360.

59. D. A. Tomalia, H. Baker, J. Dewald, et al., "A New Class of Polymers: Starburst-Dendritic Macromolecules," *Polymer Journal* 17 (1985): 117–132.

60. D. A. Markelov, A. S. Semisalova, and M. A. Mazo, "Formation of a Hollow Core in Dendrimers in Solvents," *Macromolecular Chemistry and Physics* 222 (2021): 2100085.

61. J. Höpfner, C. Klein, and M. Wilhelm, "A Novel Approach for the Desalination of Seawater by Means of Reusable Poly(Acrylic Acid) Hydrogels and Mechanical Force," *Macromolecular Rapid Communications* 31 (2010): 1337–1342.

62. O. V. Rud, J. Landsgesell, C. Holm, and P. Košovan, "Modeling of Weak Polyelectrolyte Hydrogels Under Compression – Implications for Water Desalination," *Desalination* 506 (2021): 114995.

63. V. M. Prokacheva, O. V. Rud, F. Uhílk, and O. V. Borisov, "Phase Transition in Hydrophobic Weak Polyelectrolyte Gel Utilized for Water Desalination," *Desalination* 511 (2021): 115092.

64. S.-L. Loo, L. Vásquez, A. Athanassiou, and D. Fragouli, "Polymeric Hydrogels—A Promising Platform in Enhancing Water Security for a Sustainable Future," *Advanced Materials Interfaces* 8 (2021): 2100580.

65. O. V. Rud, A. D. Kazakov, L. Nova, and F. Uhlik, "Polyelectrolyte Hydrogels as Draw Agents for Desalination of Solutions With Multivalent Ions," *Macromolecules* 55 (2022): 1763–1770.

Supporting Information

Additional supporting information can be found online in the Supporting Information section.